

Part II

Experimental activities

Chapter 5

Results and discussion

5.1 AlSi10Mg by DMLS

In this PhD thesis work, the attention was focused on the development of aluminium alloys and Aluminium Matrix Composites (AMCs). Among the aluminium alloys, AlSi10Mg0.3 from EOS GmbH (Germany) is commercially available in powder suitable for SLM/DMLS process. Its nominal composition as given by EOS datasheets is reported in table 5.1. Looking at the literature, this alloy has a composition similar to A360.2 cast alloy [95].

<i>Element</i>	Si	Fe	Cu	Mn	Mg	Zn	Ti	Al
Weight %	9-11	≤0.55	≤0.05	≤0.45	0.2-0.45	≤0.1	≤0.15	remainder

Table 5.1: Composition of AlSi10Mg alloy [3]

This alloy exhibits a relatively high flowability, which is preferred for Additive Manufacturing processes (high “castability” of the Al-Si system especially near to the eutectic). The composition of the alloy is indicated in the phase diagram reported in figure 5.1:

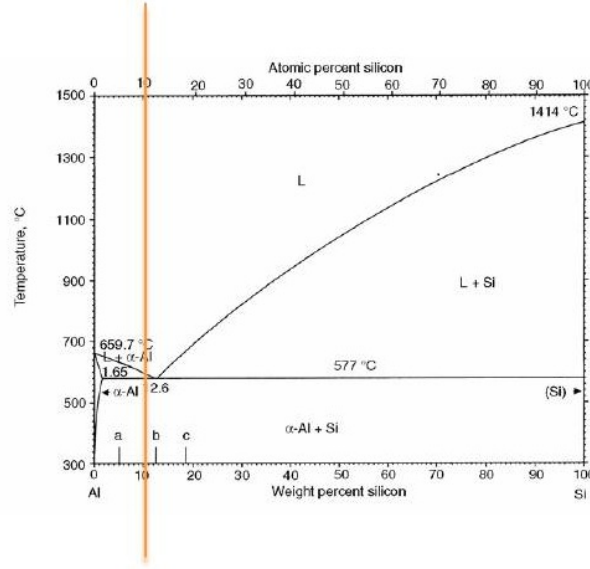


Figure 5.1: Al-Si binary equilibrium phase diagram [95]: the composition of Al-Si10% is indicated by the line.

Since DMLS is a powder bed technology, at the beginning it is fundamental to analyse the status of the powders, which are the input raw material for the fabrication of parts.

5.1.1 “Process window” of AlSi10Mg alloy: density optimization

As it was previously described in chapter 3, it was chosen to follow the well known approach of the volumetric energy density (VED) in order to take into account the combined effects of the process parameters, in particular scan speed, hatching distance, laser power on density (and so porosity) of the studied AlSi10Mg alloy. This type of work allowed to identify the optimal “process window” in terms of VED for the alloy object of the study, to minimize the porosity so enhancing the mechanical properties.

The following relation was proposed:

$$VED = \frac{P}{h_d s_s d}$$

where VED is the volumetric energy density, measured in J/mm³, s_s is the raster scanning speed of the laser beam, h_d is the scan spacing, and d is the layer thickness. This equation works when laser spot size is always larger than hatching distance. Lower layer thickness also means lower shrinkage after

melting by moving laser beam, which will increase the dimensional accuracy and surface smoothness.

To maximize the VED, the highest possible value of the laser power is used for producing metal parts. The laser power is thus set to 195 W which corresponds to 97.5% of the maximum power and guarantees a uniform continuous wave. To investigate interaction effects, the laser power is decreased also to 180 W. Regarding scanning speed and hatching distance, default values for AlSi10Mg alloy are 800 mm/s and 0.17 mm respectively. An increase of scanning speed and hatching distance improves the rate of production and decreases the VED.

Moreover, it is reported in literature that by reducing scanning speed the width of the scan line increases and by reducing hatching distance consecutive scan lines are more closely connected [28]. Thus, higher and lower values of hatching distance are selected to analyze the overlapping of scan lines. The results of parameters choice on the microstructure of the material will be discussed later.

To investigate the effect of variations of scanning speed and hatching distance on hardness and density, four levels of each parameter were selected.

Figure 5.2 shows the influence of the surface energy density (the layer thickness d is a constant value equal to 30 μm) on the hardness and the density. Considering the hatching distance of 0.25 mm, a high sensitivity of macroscopic properties is observed on the variation of the energy density. In fact, the hardness and the density increase by 23.5 % and 5.4%, respectively with a change of energy density from 0.8 to 1 J/mm². When the hatching distance was decreased from 0.25 mm to 0.17 mm and below, the hardness and density became less sensitive to the change in energy density. It is possible to identify a region, corresponding to energy density in the range 1.2 - 1.8 J/mm², in which the resulting points are concentrated.

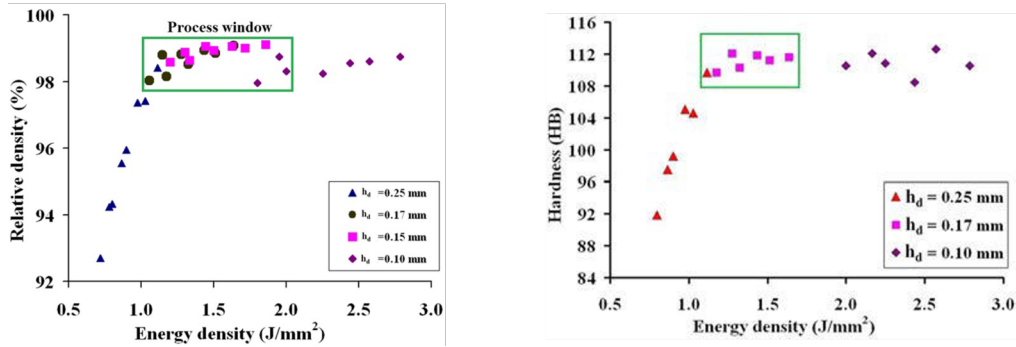


Figure 5.2: Influence of surface energy density on relative density (on the left) and on hardness (on the right) [5]

The measured average densities of the AlSi10Mg regular samples after DMLS process are summarized in table 5.2. The specimens were evaluated in three different surface finishing conditions, in particular: as DMLS, after shot peening, and after polishing, so after completely removing the roughest outer surfaces.

	<i>After DMLS</i>	<i>After Shot Peening</i>	<i>After Polishing</i>
<i>Bulk Dens. [g/cm³]</i>	2.59	2.63	2.65
<i>App. Dens. [g/cm³]</i>	2.63	2.65	2.66
<i>Total Porosity [%]</i>	3.3	2.0	1.1
<i>Closed Porosity [%]</i>	1.6	1.1	0.7

Table 5.2: Average densities of AlSi10Mg samples in different post processing conditions [96]

The calculations to estimate the total and closed porosity were made taking into account a theoretical value of 2.68 g/cm^3 . As can be observed, the layers which are relatively close to the external surfaces are more “defective” with respect to the inner ones (figure 5.3). As a consequence, the more you reduce the presence of these subsuperficial pores which are intrinsic of the process, the more the porosity evaluation is reliable.

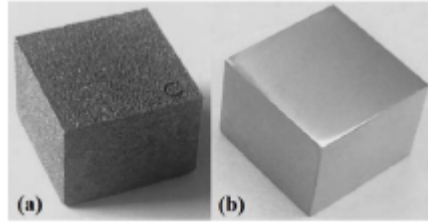


Figure 5.3: AlSi10Mg sample before (a) and after (b) polishing, so “defective” outer skins removal

For this reason the surface finishing condition affects a lot the mechanical performances of the alloy.

5.1.2 Powder characterization

Aluminium alloy samples were produced using an EOSINT M270 Xtended version machine which is available at CSHR-IIT@PoliTo. In this machine a pow-

erful Yb (Ytterbium) fiber laser system in an argon atmosphere is used to melt powders with a continuous power up to 200 W and a spot size of 100. For more details concerning the machine refer to chapter 4 of this thesis work. The aluminium powder alloy used in this study is a gas atomized one and it is produced by EOS GmbH.

Preliminary observations were performed to investigate the morphology of AlSi10Mg powder particles by using FESEM (Zeiss Supra *TM40*). The objective is first of all to verify whether the conditions of the raw powders are suitable for DMLS process, in particular from a morphological point of view. In fact, the more is the spherical morphology of the particles, the more is the good flowability and homogeneous layer distribution in the process.

Figure 5.4 shows some examples of FESEM micrographs at different magnifications of AlSi10Mg powder in the as received conditions. The AlSi10Mg particles are almost spherical and this ensures a good flowability and layer distribution of the particles themselves. The size of AlSi10Mg ranges from 1 to 45 μm with an average size around 25 μm . Some bigger clusters of dimension larger than 40 μm were also observed, due to the fact that the smallest particles tend to agglomerate to reduce their surface free energy (figure 5.4b).

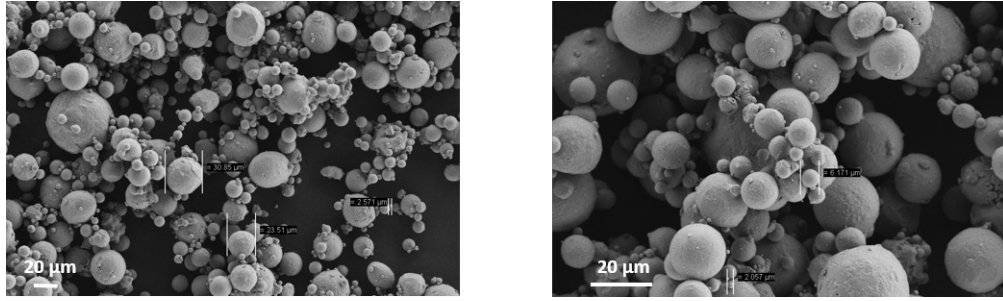


Figure 5.4: FESEM micrographs showing the morphology of AlSi10Mg powder in the as received condition

These clusters could be detrimental for the final density of the DMLS parts, considering that the layer thickness employed was of 30 μm . This tendency to agglomerate is confirmed by the granulometric analyses (Fritsch model Analysette 22 Compact) reported in figure 5.5. The diameters corresponding to 10% (d_{10}), 50% (d_{50}) and 90% (d_{90}) of the cumulative size distribution are 19.3 μm , 40.7 μm and 74.8 μm , respectively. In the graph, the frequency distribution is based on a volumetric assumption. This means that even if the small particles are far more than the bigger ones in number, their mean volume is three orders of magnitude less than the big ones: for this reason, they could not be detected and then displayed.

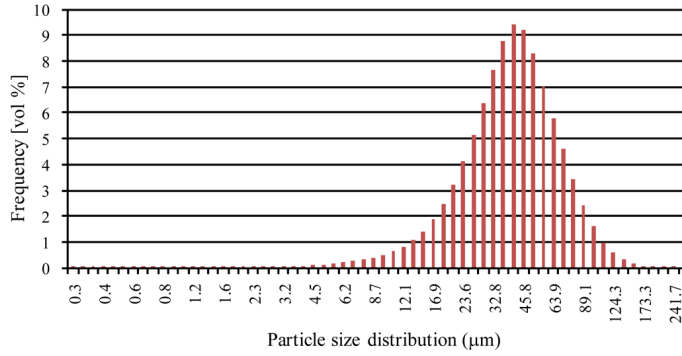


Figure 5.5: Particles size distribution of the as received AlSi10Mg powder [69]

In addition to the particles size and distribution, also their chemical composition could affect the densification in DMLS process, as observed by Olakanmi et al. [59]. The values of the chemical analyses conducted via ICP (Inductively Coupled Plasma) test are summarized in table 5.3. As it can be seen, the main alloying elements are silicon and magnesium, as expected, but it is also present an appreciable quantity of iron.

Element	Weight (%)
Si	10.08
Fe	0.16
Cu	0.001
Mn	0.002
Mg	0.35
Zn	0.002
Ti	0.01
Al	balance

Table 5.3: Chemical composition of aluminium alloy powder as determined by ICP test [69]

The choice of the process parameters required to obtain a part with the best surface finishing and highest density was described in a previous study from the same research group in which this thesis work was pursued [31]: the values of these parameters are given in table 5.4. As explained in that study, the machine uses different parameters for the core of a part and for the outer surfaces: the lower and upper ones parallel to the building plane, and the lateral ones, called contour.

Parameters	Skin	Core	Contour
Scan speed (v) [mm/s]	900	800	900
Laser power (P) [W]	120	195	80
Hatching distance (h_d) [mm]	0.1	0.17	–
Layer thickness [μm]	30	30	–

Table 5.4: DMLS process parameters in use [69]

In addition, concerning the scanning strategy associated to the core and to the skin, a certain degree of rotation between two successive layers was proved to lead to a better overlapping. This should make the properties of the parts obtained more isotropic in comparison with more conventional scanning strategies made of layers with unidirectional vectors. The evaluation of the mechanical properties of parts by DMLS was pursued on specimens built in four different orientations and with different surface finishing conditions. Then, the effect of the DMLS process on the microstructure of the components was evaluated by optical and electron microscopies.

5.1.3 Mechanical properties evaluation

All specimens for mechanical characterizationa were fabricated using the mentioned optimized parameters and scanning strategy. The orientations considered are along the z axis, the building direction, and along three directions on the building platform (in the x/y plane): parallel to the direction of the powder deposition, along the normal axis to it and at 45° between them, as it is illustrated in the scheme in figure 5.6. Samples of rectangular shape and $50 \times 10 \times 5$ mm size were produced to analyze the density, hardness and elastic modulus. Considering tensile tests, five specimens for each orientation were built according to the standard ASTM E8M.

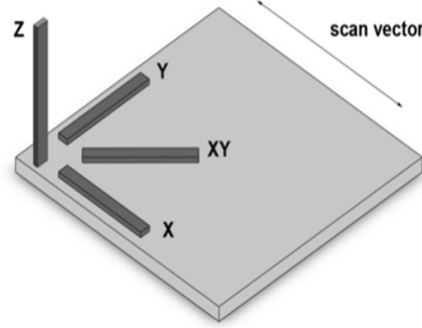


Figure 5.6: Scheme of the four different orientations considered for the fabrication of AlSi10Mg specimens

Due to the high thermal gradients, this process fabricates parts with high residual thermal stresses. In order to avoid the warping of the parts, before removing them from the building platform, it is necessary to perform an annealing for 2 h at 300 °C. The samples were then shot-peened by using an Ecoblast/F machine from Silco S.r.l. (Italy), to improve the surface quality and finishing. In this study, glass beads of 200 μm mean diameter with an air pressure value of 8 bar for several seconds were used. These beads produce a clean, bright, satin-finished surface, with an R_a average value of 3 μm without dimensional change or contamination of the parts [96].

Concerning mechanical characterization, the samples were then polished down to diluted silica suspension paste to allow Vickers microhardness measurements, performed by a Leitz instrument (the load was set to 50 g for 30 s): fifteen measurements were repeated to calculate a mean hardness value for each orientation. Elastic modulus was evaluated by an impulse excitation technique involving the analysis of the transient natural vibration, by means of a GrindoSonic MK5 instrument, according to the standard ASTM C1259. The results of these measurements are reported in the following table 5.5:

Density (g/cm^3)	Residual Porosity (%)	Hardness (HV)	Young's Modulus E (GPa)
2.66	0.8	105 ± 5	73 ± 1

Table 5.5: Microhardness and elastic modulus evaluations on AlSi10Mg alloy

Tensile tests were performed on an EASYDUR 3MZ - 5000 testing machine, with a free-running crosshead speed of 2 mm/min. The strain was measured by a piezo-electric extensometer. After rupture, the fracture surfaces were observed by FESEM. Moreover, ASTM E 23 was finally followed to carry out Charpy impact test of AlSi10Mg samples by DMLS. Two different types of specimen

geometry were tested, with V-notch and without notch. The samples with V-notch and without notch were produced in two orientations, in particular along the x/y plane, and also in the z direction. The fracture surfaces were then observed by FESEM.

In the following table 5.6 the mean obtained values from the pursued tensile tests are reported.

<i>Material</i>	<i>Orientation</i>	<i>Yield Strength</i> $\sigma_{0.2}$ (MPa)	<i>Ultimate Tensile Strength</i> σ_{UTS} (MPa)	<i>Elongation at break</i> (%)
<i>AlSiMg after DMLS</i>	<i>xy plane</i>	245	330	6.6
	<i>z axis</i>	233	329	4.3
<i>A360 F*</i>	-	170	317	5

Table 5.6: Mean values of tensile properties of AlSi10Mg specimens produced according to the standard ASTM E8M along different orientations, compared to the A360.2 alloy realized by conventional casting [69]

AlSi10Mg0.3 tested specimens showed an isotropic behavior when built on the x/y plane. This is due to the scanning strategy consisting of the rotation of each layer of 67° with respect to the previous one. Considering the specimens built along the z axis direction, the properties resulted to be relatively lower. In figure the representative trends of stress-strain curves are illustrated, for each considered orientation. There is a high reproducibility of the results. In figure 5.7, examples of stress-strain curves of a specimen built along the four different considered directions are reported. Considering the tangent to the curve in the elastic region, the values for the elastic modulus could also be estimated: it was confirmed that they are in good agreement with the results obtained by the used impulse excitation technique.

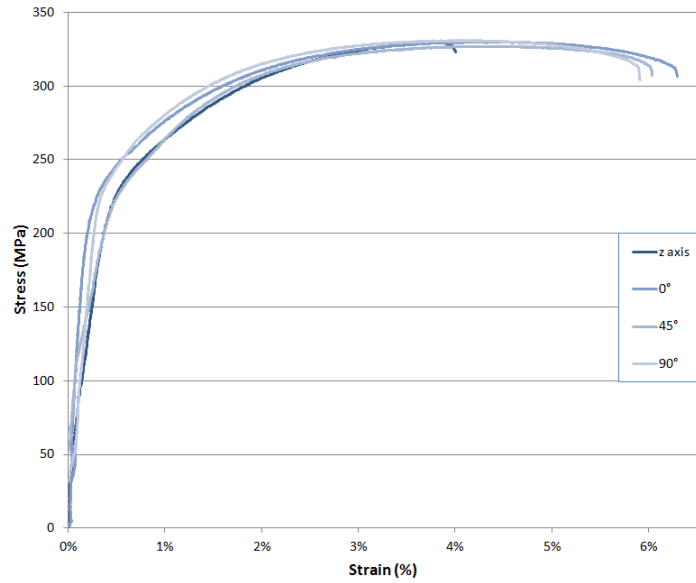


Figure 5.7: Typical stress-strain curves for aluminum alloy DMLS specimens built along four different orientations [69]

Fracture surfaces after tensile tests were investigated by FESEM, as reported in figure 5.8. As can be seen, the surface is covered by very fine dimples, clearly visible only at high magnification. On the left image there can also be observed two little concave zones probably related to two spherical particles not completely melted. At higher magnification is possible to appreciate the very fine dimension of the microstructure, with presence of particles of tens of nanometers.

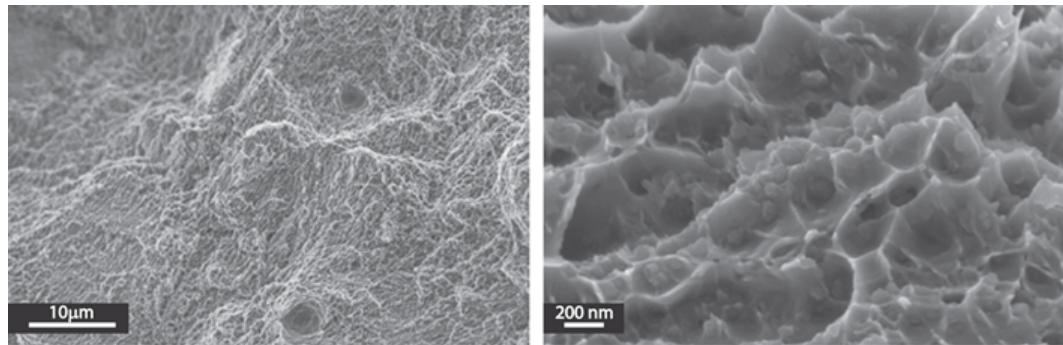


Figure 5.8: FESEM images of an aluminum alloy DMLS fracture surface covered by sub-micrometric voids and dimples with a nanometric size

The AlSi10Mg samples with V-notch and without notch were produced in two orientations: in the x/y plane and also in z direction. Specimens with V-notch were tested in two different surface finish conditions, (i) as built and (ii) shot peened. Samples without notch were tested in three different surface finish conditions: (i) as built, (ii) shot peened and (iii) after polishing, as reported in figure 5.9.

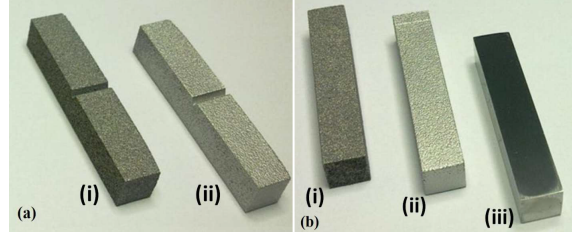


Figure 5.9: Charpy test specimens with V-notch (a) and without notch (b), where (i) as built, (ii) shot peened and (iii) after polishing [98]

The results of Charpy tests on samples with V-notch are listed in table 5.7. The impact energy absorbed by the specimens in as built and after shot peening conditions are comparable. The samples oriented in the x/y plane absorbed higher energy than the specimens oriented along z direction.

Finish condition	Impact Energy (J)			
	mean	S.D	mean	S.D
As built	8.3	0.2	4.7	0.7
Shot peened	7.9	0.1	4.1	0.8
Orientation	XY plane		Z direction	

(a)

Finish condition	Impact Energy (J)			
	mean	S.D	mean	S.D
As built	32.6	0.9	19.6	0.7
Shot peened	31.8	2.0	19.6	0.9
After polishing	40.7	4.3	23.9	0.2
Orientation	XY plane		Z direction	

(b)

Table 5.7: Charpy impact energy of specimens presenting the V-notch (a) and without notch (b) [97]

The impact energy absorbed by the AlSi10Mg specimens produced by DMLS is superior than that of die cast aluminium alloy parts, even though the surface roughness of DMLS specimens is in any case higher than die cast components.

Comparing the results from testing specimens with V-notch and specimens without notch, samples without notch absorbed higher energy, as expected. Moreover, the samples after polishing absorbed relatively higher energy than the ones in as built and shot peened conditions. This could be due to the high roughness of the specimens as fabricated by DMLS process.

In fact, the impact energy is influenced by subsuperficial defects which are concentrated at the interface between the outer skins and the core. Figure 5.10 shows the fracture surfaces of a Charpy test specimen oriented in the x/y plane.

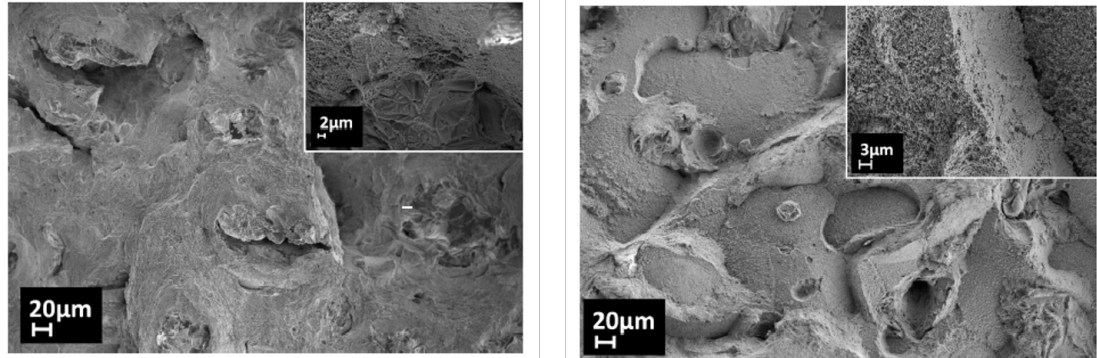


Figure 5.10: FESEM observation fracture surface of Charpy specimen oriented in x/y plane (on the left) and the fracture surface of a specimen oriented along the z direction (on the right) [98]

The fracture surface consists of both ductile and brittle regions. In particular, the ductile region consists of very fine dimples and microvoids. Fracture surface of Charpy specimen oriented along the z direction is illustrated in figure 5.10(b). The topography of the fracture surface for the z direction specimen is different from the x/y oriented one. This could be due to the nature of the process and orientation of the layers with respect to the length of the specimens. In fact, the Charpy hammer impacted perpendicular to the layers in the x/y plane oriented specimen, and parallel to the layers in the z direction oriented ones.

5.1.4 Microstructural characterization

Concerning the microstructural analyses, the DMLS samples were cross-sectioned perpendicular and parallel to the building platform, then polished down to colloidal silica suspension (size $0.05\text{ }\mu\text{m}$) and etched with Weck's reagent (KMnO_4 and NaOH mixed in proportion in distilled water) for 15 s; after that, they were observed by an optical microscope and by FESEM. All the microstructural images then refer to the core of the parts.

The AlSi10Mg samples microstructure was initially analyzed by optical microscopy. Figure 5.11 shows micrographs of two cross sections: a section parallel to the build direction, indicated by the black arrow (figure 5.11 a), and a section perpendicular to it (figure 5.11 b).

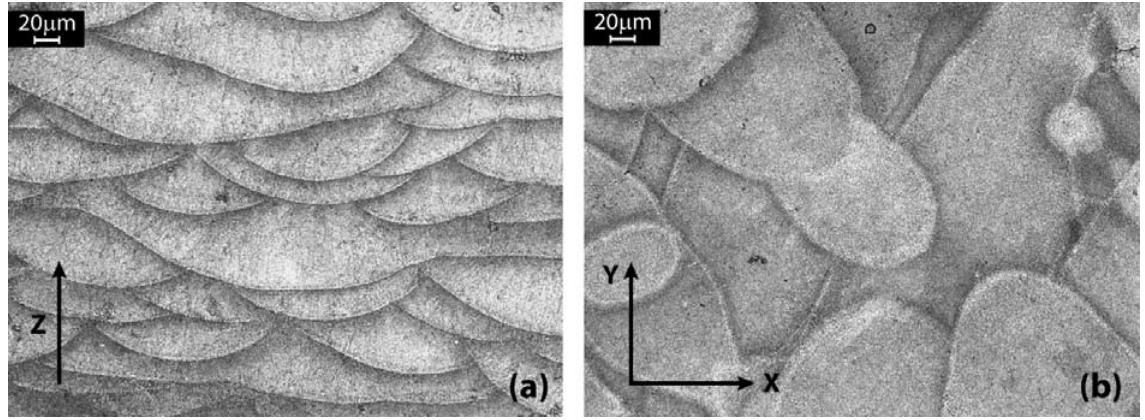


Figure 5.11: Optical microscope images of an aluminum alloy sample after etching with Weck's reagent: (a) a section along the build direction (z axis); a section parallel to the powder deposition plane (xy-plane) [69]

The laser beam power is modulated in such a way as to ensure that the new deposited layer is completely melted and reaches the previous layer, so remelting in a good joining of the layers (wetting of the layer underneath) at the same time. Hence, considering a mirror like finished section along the build direction, these melt pools are all oriented in the same way (figure 5.11a), being a section made by the superimposition of successive layers. The Weck's etchant solution results to be very effective to highlight the melt pools at the optical microscope. However, due to the described scanning strategy adopted in this study and by taking into account the cited remelting, the volumetric shape of these melt pools is not exactly half-cylindrical. Consequently it is not possible to define their mean depth. On the opposite, considering the polished and etched section parallel to the powder deposition plane, it could be assumed to observe the cross-section of the melt pools of different successive layers (figure 5.11b). Moreover, due to the different depth, their contours overlap originating shapes with irregular geometries, depending at which "height" the sample was cut before the metallographic preparation.

Looking at the micrographs of figure 5.12, even if some porosity is visible in the samples investigated, the pores dimension is very little. Going at higher magnifications, it is possible to appreciate their mean size: in figure 5.12 a, two pores are visible, with a dimension of about 20 μm, while figure 5.12 b is focused on a single melt pool and its region of contour. As can be observed, the rapid and localized melting and cooling of DMLS originate very fine microstructures.

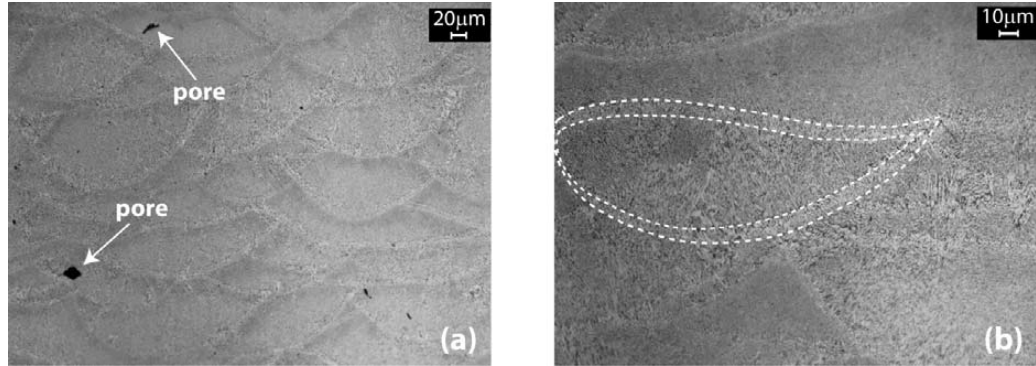


Figure 5.12: Optical microscope images after Weck's etching showing: (a) the presence of pores and at a higher magnification; (b) the shape of a melt pool with its contour [69]

As published by Manfredi et al. in 2013 [69], in order to appreciate this small grain size, the section along the build direction was observed by FESEM, focusing on a region between two melt pools, as shown in figure 5.13a. The area inside the white parallel lines corresponds to the melt pool contour (mpc), with a mean height of about 8 μm. At higher magnifications, from figure 5.13 (b - d), it can be seen that the three regions (mp1, mp2 and mpc) are characterized by a fine cellular-dendritic structure made by agglomerates of grains with mean diameters of 80 nm or less. It was found that these agglomerates are different in length, thickness and aspect ratio in the three regions. According to Olakanmi et al. [59] it can be assumed that there is little or no free-energy barrier to the phase transformation from liquid to solid. It is due to the complete wetting of the substrate by the molten metal and the nearly ideal interface provided by the partially melted heat affected zone (HAZ) grains at the fusion boundary. In this way, the grains grow epitaxially, and the grain direction is parallel with the local conductive heat transfer, as shown in figure 5.13 (b - d).

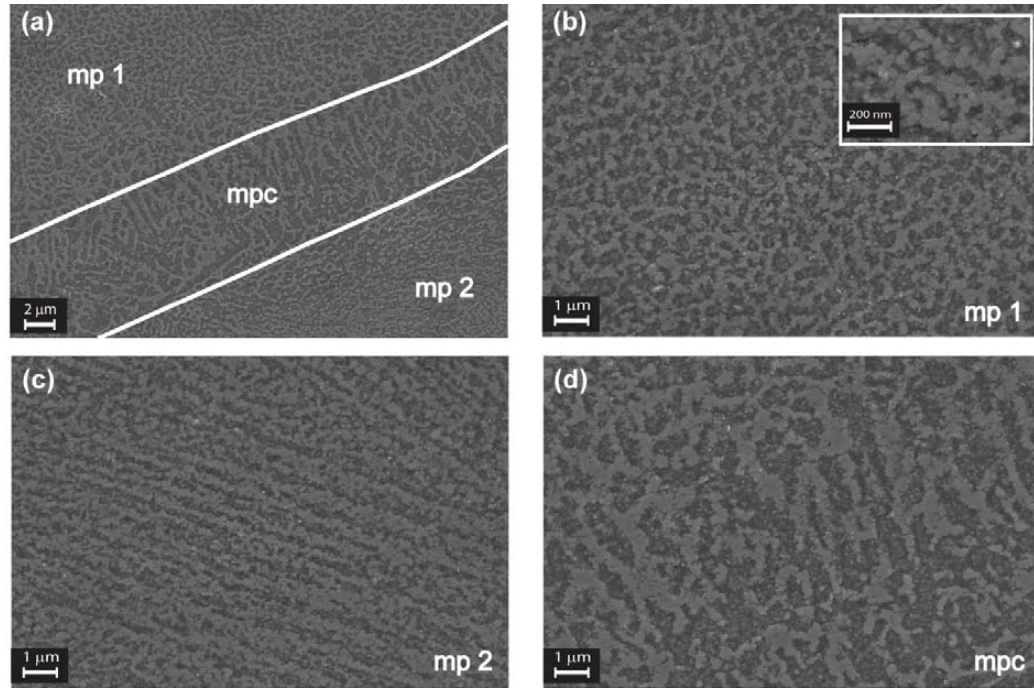


Figure 5.13: FESEM images of an aluminum alloy DMLS sample after etching with Weck's reagent, sectioned along the z axis: (a) mp1 and mp2 are areas of two adjacent melt pools, while the region delimited by the white lines correspond to the melt pool contour (mpc); (b–d) the three regions at higher magnifications. In the inset, it possible to observe the nanometric grain size [69]

During the DMLS process, taking into account the short interaction times and high conductive heat transfer rate, a very fine microstructure originates. The exposure period of the laser irradiation is in the range of milliseconds. In figure 5.14 it can be observed that the dendritic predominant phase, constituted by the α -Al grains which present a submicrometric scale, contains a large number of darker grains, most probably of silicon, which present a nanometric size.

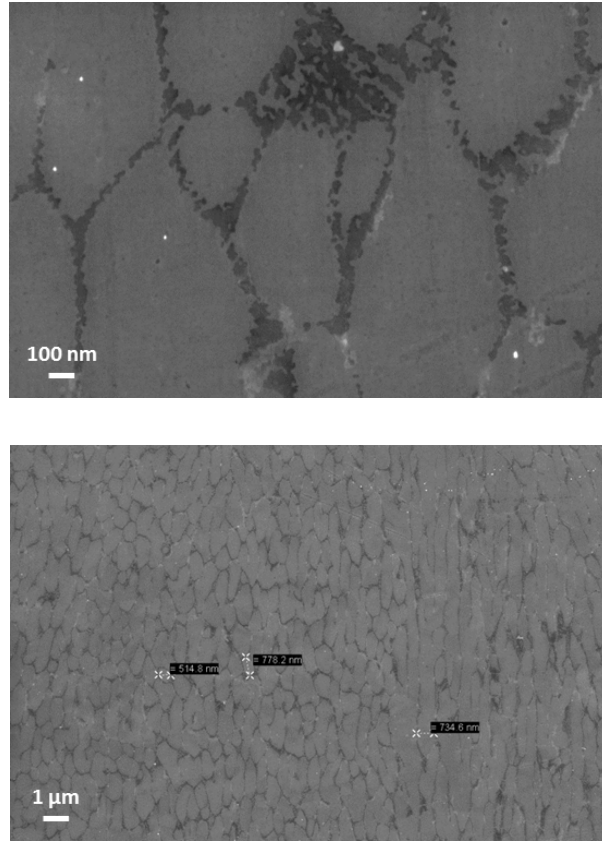


Figure 5.14: FESEM observation of the nanometric grains of Si (darker structure) in the submicrometric α -Al phase (brighter)

Figure 5.15 (a) and (b) shows the microstructure of AlSi10Mg sample produced by orienting scan tracks only along x axis (refer to chapter 4 for the different building strategies description).

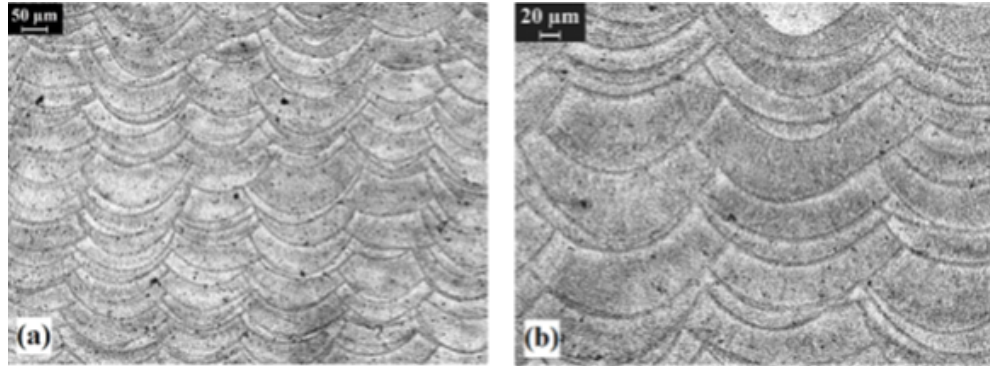


Figure 5.15: Optical micrographs of AlSi10Mg specimen produced by orienting scan tracks along x axis, after etching with Weck's reagent [5]

It can be observed that the shape of scan tracks is crescent or elliptical. However, this specimen had a higher porosity with respect to the ones obtained with the default scanning strategy. Therefore, the default scanning strategy with 67° is generally chosen to produce AlSi10Mg specimens for the evaluation of the mechanical properties.

The very high cooling rates promote a great undercooling, thus producing fine grains and a gradual change in the solidification regime from dendritic to cellular-dendritic. At the same time it is difficult to investigate the nature of the relatively small amount of precipitates which formation is mainly due to the non-equilibrium conditions and the solidification conditions associated with the DMLS process. As reported by Manfredi et al. in 2013 [96], in order to investigate the different phases present in the AlSi10Mg samples and to validate the microstructural description, XRD analyses were performed on cross sections of polished samples without etching and the pattern obtained is reported in figure 5.16

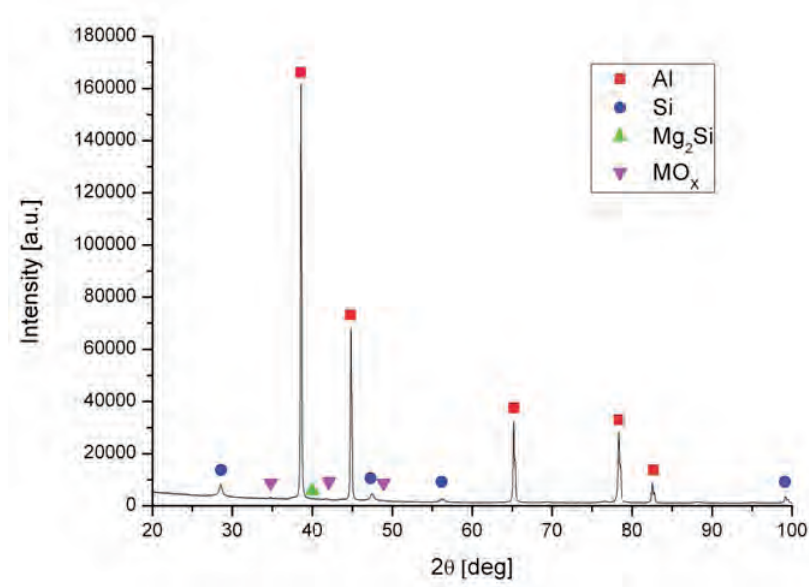


Figure 5.16: XRD pattern from AlSi10Mg specimen processed by DMLS

It is possible to identify the typical peaks which correspond to the Mg_2Si phase, but their intensity is relatively low if compared to Al and Si. It is interesting to note the presence of some mixed metal oxides (indicated by MO_x), in which M could be Al or Mg or both of them, as in case of a mixed oxide.

It can be concluded that the mechanical properties without the need of a further heat treatment after DMLS, as usually happens with casting alloys, are superior.

5.1.5 Heat treatment: T6 cycle characterization

A T6 cycle of solution annealing, quenching and then age hardening was pursued on a series of AlSi10Mg tensile specimens. The phases were the following:

- solution treatment at 530 °C for 5 hours;
- quenching in water for 20 seconds;
- age hardening at 160 °C for 12 hours.

Few specimens were fabricated for the characterization of heat treated AlSi10Mg. The results of the tensile tests and Vickers microhardnesses are reported in the following table 5.8, which also contains the comparison with AlSi10Mg alloy in the stress relieved condition:

Heat treatment	YTS [MPa]	UTS [MPa]	E [%]	Durezza [HV]
T6	244 ± 7	278 ± 2	4.0 ± 0.8	118.9 ± 5.7
Stress relieved	245	330	6,6	105 ± 5

Table 5.8: Summary of the tensile tests and microhardness results

From the microstructural analysis you can observe that there is a tendency of the grain size to grow with respect to the stress relieved AlSi10Mg alloy. In figure 5.17 some optical micrographs at different magnifications are reported to support this:

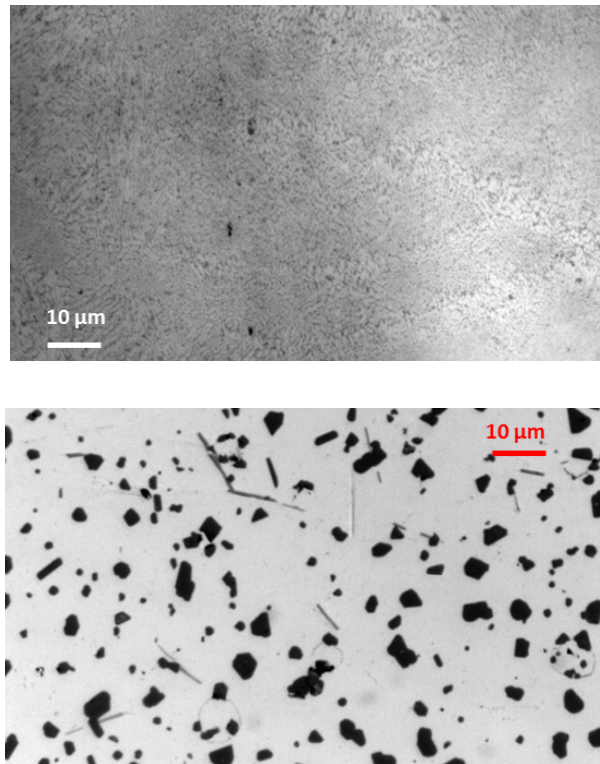


Figure 5.17: Optical micrographs of stress relieved AlSi10Mg (on the left) in comparison with after T6 AlSi10Mg (on the right)

It could be assumed that a T6 cycle makes the microstructure more homogeneous, because there are no longer the melt pool regions typical of DMLS

process. The hardness increases and the elongation to rupture simultaneously decreased.

5.2 AlSi10Mg/SiC (10% in wt.) composite

The ceramic materials generally used as particulate reinforcements in the field of composites are Al_2O_3 , SiC, B_4C and recently also TiB_2 , TiC emerged as potential candidates. Topcu et al. recently investigated the mechanical performances at high temperature of composites with different compositions reinforced varying weight percentages of micro- B_4C particles, fabricated by powder metallurgy and subsequent sintering [84]. In 2008, Kerti et al. proposed a solution to promote the wettability between the ceramic reinforcement and aluminum melt during casting phase [85].

However, the most used ceramic is SiC: many literature works were recently published on the preparation and characterization of composites containing it. In fact SiC exhibits:

- very high strength and melting temperature (2730 °C);
- excellent hardness and wear resistance.

For example, El-Kady et al. contributed to the characterization of Al-SiC composites in different weight percentages, obtained by powder metallurgy, showing that the decrease in SiC average particle size as well as the increase in content, improved mechanical properties, in particular hardness and consequently compressive strength [99].

In the case of DMLS process, silicon carbide was the most studied second phase, due to its interesting hardness, stiffness and thermal properties. In 2008 Simchi et al. published an investigation of AlSi7Mg0.3-SiC composites by DMLS [86].

In the Al-SiC system, one of the most serious detrimental issues is the possible reaction between the aluminum matrix and the silicon carbide reinforcement. In 1998 Lee et al. reported a thermodynamic study by combining together a theoretical model based on calculations and a collection of experimental data, with the aim to suppress the reaction between the two constituents [100]. It is proved there that by increasing Si activity by dissolving a certain amount of Si into the aluminum matrix, the Al activity is reduced, resulting in the desired suppression of the reaction.

The predicted results vary significantly depending on the authors, as reported in figure 5.18.

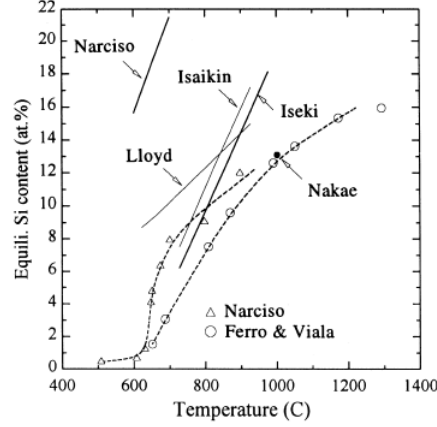
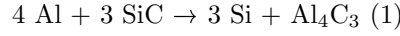
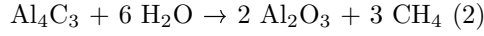


Figure 5.18: Equilibrium Si content in the Al-SiC composite as a function of temperature [100]

This reaction is well-known in the literature and brings to the formation of the aluminum carbide Al_4C_3 following this equation (1):



Aluminum carbide is a brittle carbide, that generally reduces the properties of the composites. Anyway another problem is its reaction with water, that forms aluminum oxide and methane following the reaction (2):



Thus, if water penetrated inside a composite containing aluminum carbide, for instance through porosity or cracks, then gas is formed and pressure locally builds-up, bringing to the disruption of the composite itself. In order to contrast this dangerous Al_4C_3 formation, the basic principle is to enhance the Si activity by solving a proper amount of Si in the Al matrix, as previously mentioned. In the literature it is suggested that 10% of Si is sufficient to prevent the reaction between aluminum and silicon carbide in the 700 - 900 °C temperature range.

5.2.1 Starting material

The composite powder was obtained by mechanically alloying a mixture of the two different powder constituents. In practice the ex situ approach, which literature advances were discussed in chapter 3, was employed to fabricate this ceramic reinforced aluminium matrix composite powder. In fact the composite powder was realized by simply mixing the AlSi10Mg and SiC powders in the desired weight percentages in ceramic jars without the use of any additional grinding medium (milling technique).

AlSi10Mg alloy powder used in the composite fabrication is always the commercial gas atomized one by EOS GmbH, with a nominal density of 2.68 g/cm^3 . The powder particles characterization of this alloy was described in the previous section. Summarizing the results, their morphology is quite spherical with a regular shape, ranging in dimensions from 1 to $44 \text{ }\mu\text{m}$, with an average which could be set around 21 to $27 \text{ }\mu\text{m}$. To help go further two images at different magnification taken by FESEM showing the morphology of the used powder are reported in figure 5.19.

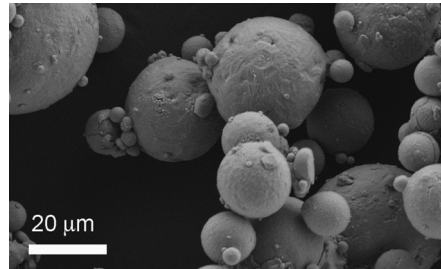


Figure 5.19: FESEM observation of AlSi10Mg starting raw powders

The other constituent is the ceramic discontinuos reinforcement, which consists of the used α grade submicrometric SiC, produced by H. C. Starck (Germany): table 5.9 summerizes the properties of the type of SiC powder in use.

Product Type	Powder Particle Size $d_{50} \mu\text{m}$	Specific Surface Area (BET) m^2/g
STARCERAM * S raw ceramic powder		
Grade UF 5	2,0	4 - 6
Grade UF 10	0,7	9 - 11
Grade UF 15	0,55	14 - 16
Grade UF 25	0,45	23 - 26

Table 5.9: Properties of α grade SiC particles by H.C. Starck [103]

As it is underlined, SiC powders of the type in use have got a mean particle size of about $0.55 \text{ }\mu\text{m}$. In this case the particles are too small to be able to evaluate their density by picnometry means, since this technique presents a intrinsic limit in terms of particle size detection. From the observations taken by FESEM the particles present an angular shape and show a little tendency to agglomerate: you can refer to figure5.20 below in which the images are reported.

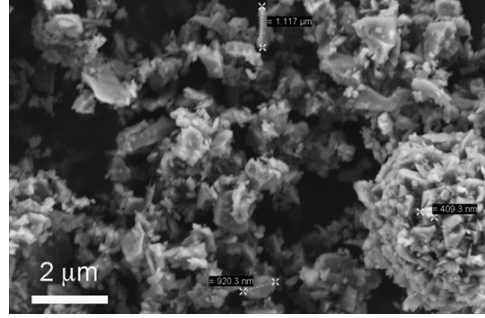


Figure 5.20: FESEM image of submicrometric SiC particles

Figure 5.21 shows the composite powders obtained after ball milling as observed by FESEM.

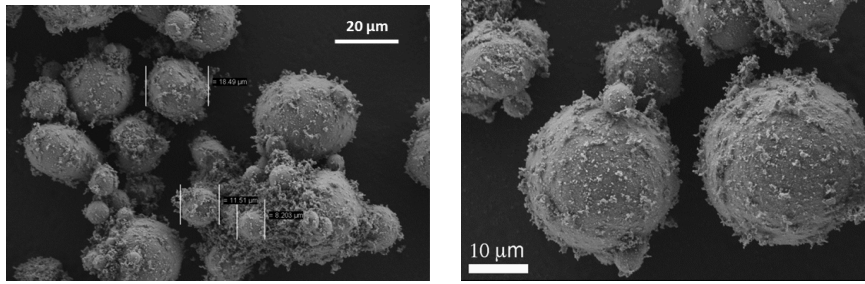


Figure 5.21: FESEM images of the composite powders after mixing AlSiMg with submicrometric SiC (10%wt.)

SiC particles are relatively smaller and tend easily to agglomerate to reduce their surface free energy (refer to figure 5.20). The AlSi10Mg particles alone (figure 5.19) are mainly spherical, with some satellites due to agglomeration of finer particles. The observation of the composite powders (figure 5.21) shows that the SiC particles cover the aluminum particles with a loosely bound surface layer, so that the composite powders have approximately the same shape of the AlSi10Mg ones. No powder deformation due to the mechanical mixing could be directly observed, and the SiC powder appears to be well distributed on the surface of aluminum.

The laser granulometry technique was carried out on the composite powder with the aim to understand how the granulometry of the prepared mixture would change in comparison with the matrix alone (figure 5.22). In this graph the measurements of laser granulometry are based on volumetric assumptions. As a result the composite presents d_{10} , d_{50} and d_{90} values of 13.0, 30.2, and 54.4 μm , respectively.

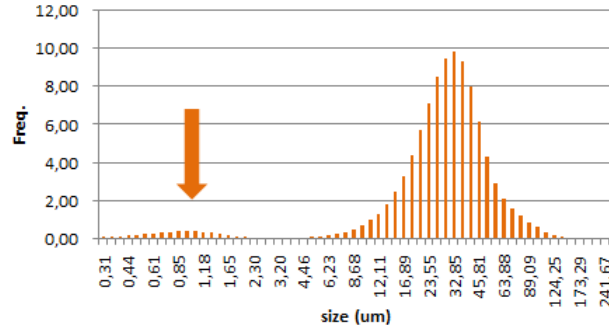


Figure 5.22: Laser granulometry resulting diagram on Al/SiC composite powder

On the whole, the composite powders were expected to behave similarly to the pure metal one, confirming the choice of avoiding deformation of the metal during the mixing of the two powders. The increase of friction between composite powders due to the presence of the ceramic coating and to the interaction of the rough surfaces should have been limited due to the large ratio between the size of the metal and the ceramic particles. However, the AlSi10Mg particles covered by this sort of ceramic fluff presented a different behaviour. In particular during the spreading phase of the powder on the build platform the flowability of the composite system revealed to be much reduced in comparison with the flowability of AlSi10Mg powder. This phenomenon occurred for the very first deposited layers, and was monitored to be reducing as the building process continued. It was observed that the already spread powder bed acts as grip for the subsequently spread particles.

In order to quantify these occurring phenomena, flowability measurements were carried out. However, the technique presents a bottle neck, because it can not reach the too low flowability of these powders for DMLS.

5.2.2 Density and porosity evaluation

To understand the combined effects of DMLS process parameters on the densification of the fabricated composite, cubic specimens of 15 mm side were fabricated by using different combinations of the building parameters, in particular laser power and scanning speed. In fact hatching distance was kept constant at the default value of 0.17 mm, which is the optimal value for the realization of dense AlSi10Mg alloy parts, as it was concluded in the previous section. Examples of the cubic samples which were used to investigate the densification of the Al/SiC composite are reported in figure 5.23.

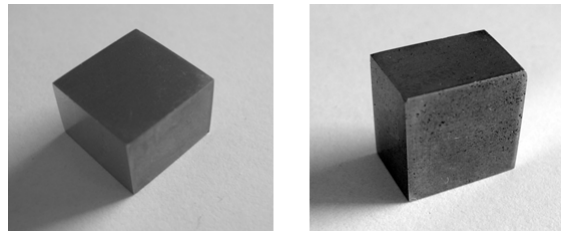


Figure 5.23: Examples of cubic AlSi10Mg/SiC composite samples fabricated for density evaluation

As it can be seen, the samples were polished in order to remove the defective outer skin, being able to evaluate the effective internal porosities of the examined material. In this way, you could avoid to take into account the roughness which is essentially intrinsic in DMLS/SLM process.

As well as the AlSi10Mg alloy, the Volumetric Energy Density (VED) evaluation was used to properly define the best window of process parameters. In table 5.10 are summarized the 25 different combinations which were analysed. The samples which are put in evidence with deleted rows were not successfully fabricated, because of a failure during the building process.

Sample	Power [W]	Scan Speed [mm/s]	Hatching distance [mm]	VED [l/mm3]
1	130	500	0,17	50,98
2	150	500	0,17	58,82
3	165	500	0,17	64,71
4	180	500	0,17	70,59
5	195	500	0,17	76,47
6	130	600	0,17	42,48
7	150	600	0,17	49,02
8	165	600	0,17	53,92
9	180	600	0,17	58,82
10	195	600	0,17	63,73
11	130	700	0,17	36,41
12	150	700	0,17	42,02
13	165	700	0,17	46,22
14	180	700	0,17	50,42
15	195	700	0,17	54,62
16	130	800	0,17	31,86
17	150	800	0,17	36,76
18	165	800	0,17	40,44
19	180	800	0,17	44,12
20	195	800	0,17	47,79
21	130	900	0,17	28,32
22	150	900	0,17	32,68
23	165	900	0,17	36,96
24	180	900	0,17	41,22
25	195	900	0,17	45,48

Table 5.10: VED evaluation for different process parameters combination of Al/SiC 10%wt. composites

Five levels of laser power were chosen: 130 W, 150 W, 165 W, 180 W and 195 W, respectively. The scanning speed was varied ranging from 500 up to 900 mm/s by 100 mm/s step.

First of all, after grinding the samples with abrasive papers to reach the suitable surface conditions of figure 5.23, it was required to calculate a reliable density value of the composite to keep it as a reference.

Hence, the theoretical density of the composite was estimated through the rule of mixture, using the value of 2.67 g/cm³ for AlSi10Mg (this value was for the specific batch in use), and assuming the density of used SiC powder equal to 3.2 g/cm³, thus obtaining a value of 2.71 g/cm³ as a reference for the composite. In terms of equations this is the rule of mixture:

$$\frac{1}{\rho_{composite}} = \frac{f_{reinf}}{\rho_{reinf}} + \frac{f_{matrix}}{\rho_{matrix}}$$

where f_{reinf} is the percentage in weight of the reinforcement (so equal to 0.1 in this case), and on the opposite f_{matrix} is the matrix weight percentage (equal to 0.9).

The bulk (or geometrical) density was calculated for each fabricated sample by following the method which was described in detail in chapter 4, in particular with reference to the equation (9), which is very useful in general to calculate the

bulk density of a part which does not present a completely regular shape. Each weighting operation (in air, in distilled water and of the dried sample after the weighting in water) was repeated three times in order to reduce the experimental deviations of the data.

Once the whole set of samples was weighted in the three ways, the porosity levels could be calculated by using the equations (6) and (7) which you can find in chapter 4, which allow to calculate open and closed porosities, respectively. The total porosity level could be calculated by simply sum the two previously obtained values. The results are summarized in table 5.11:

Sample	VED [1/mm ³]	Porosity open (%)	Porosity closed (%)	Porosity total (%)
1	50,98	0,19	6,50	6,70
2	58,82	0,09	3,39	3,48
3	64,71	0,51	2,83	3,34
4	70,59	0,37	2,81	3,19
5	76,47	0,23	2,91	3,14
6	42,48	1,80	9,14	10,94
7	49,02	0,23	4,91	5,14
8	53,92	0,31	3,31	3,63
9	58,82	0,36	2,96	3,32
10	63,73	0,34	2,61	2,95
11	36,41	1,02	10,59	11,61
14	50,42	0,31	3,72	4,03
16	31,86	2,04	12,79	14,83
18	40,44	0,37	7,28	7,65
21	28,32	7,16	10,45	17,62
25	42,48	0,29	4,33	4,62

Table 5.11: Percentage of porosity with associated VED values for the Al/SiC characterized samples

In addition, the porosity levels were also evaluated with the second proposed method of chapter 4, based on optical micrographs analysis, so resuming, by counting the fraction of pores present on a series of cross-sections of the material through the help of an image analysis software. Table 5.12 summarizes the obtained values.

	1	2	3	4	5	6	7	8	9	10	11	14	16	18	21	25
1	6.64	1.07	1.06	1.66	0.44	7.57	3.29	2.63	1.58	0.84	9.62	3.15	16.47	6.77	15.86	1.51
2	8.13	2.52	3.14	2.16	0.69	10.96	3.01	1.54	1.71	0.73	11.67	3.52	12.05	6.38	19.30	1.72
3	6.54	3.42	2.11	1.23	0.54	6.67	3.49	2.36	1.11	0.98	8.46	3.29	20.01	8.70	18.20	2.05
4	6.02	1.13	2.40	1.44	0.57	9.17	3.58	2.28	1.51	0.74	9.22	2.74	18.39	6.28	15.92	2.03
5	6.89	1.64	2.24	1.76	0.62	11.64	2.99	3.12	0.99	0.81	12.67	2.12	16.97	6.62	16.54	3.10
6	5.35	1.52	1.77	2.25	0.53	6.72	3.45	1.48	0.90	0.90	12.19	1.84	14.84	5.50	16.37	2.45
7	5.67	1.11	1.54	1.42	0.63	9.94	4.24	2.29	1.04	0.65	11.51	1.80	19.97	5.53	16.59	2.75
	6.46	1.77	2.04	1.70	0.57	8.95	3.44	2.24	1.26	0.81	10.76	2.64	16.96	6.54	16.97	2.23

Table 5.12: Percentage of porosity for the Al/SiC samples by DMLS calculated by optical microscopy method

The values of porosity obtained by this method are values of total porosity.

As you can observe, for each sample seven micrographs were taken in order to have a more accurate statistics, because the intrinsic error of the method gets reduced by increasing the number of selected micrographs. Moreover, in figure 5.24 the micrographs taken at 50x magnification of cross-sectioned sample 10 along the x/y plane are reported as a clarifying example. The scale bar had to be removed in order to distinguish clearly the porosity.

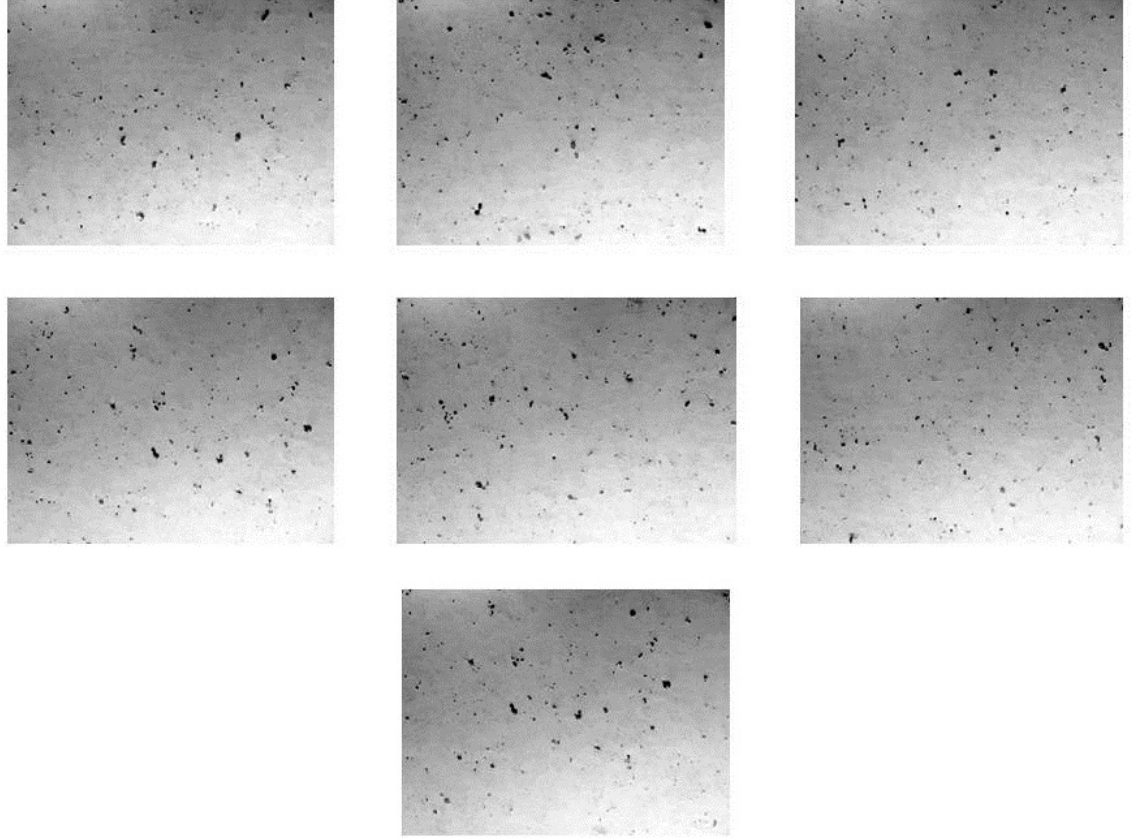


Figure 5.24: 7 optical micrographs (sample 10) of the cross-sections along the x/y plane for porosity evaluation

Then, the values of the total porosity obtained by the two different methods (by weightings and by optical microscopy) could be compared by plotting the values themselves versus the VED values, in a summarizing graph which is reported in figure 5.25 below.

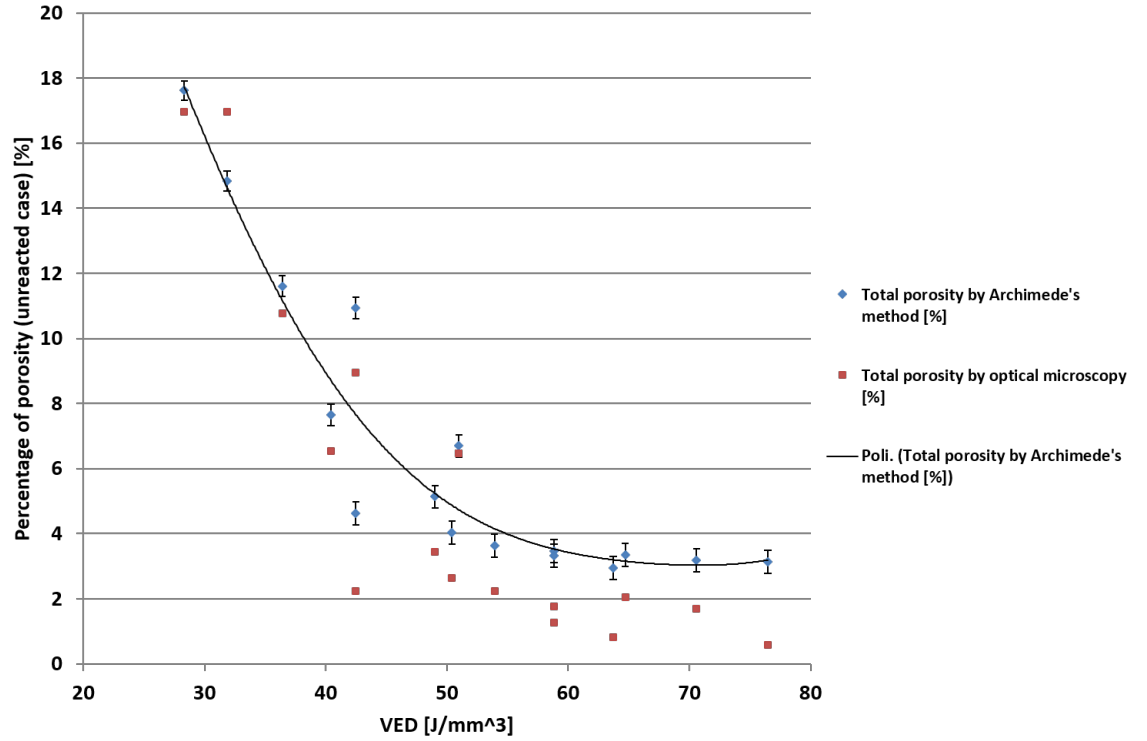


Figure 5.25: Percentage of total porosity obtained by two different methods for Al/SiC composites by DMLS

The obtained results can be considered really good in particular with respect to the previous studies in literature: in fact, Ghosh et al. [87] for Al-SiC composites (with different matrixes) by DMLS obtained residual porosities of about 14%.

The composite chemical composition was investigated by means of XRD analysis: silicon carbide showed a marked reaction with aluminum alloy. For more conventional processes, this behavior was somewhat unexpected. In fact, when 10% Si content alloys are used (see the introduction to this paragraph), generally the reaction (1) reported is suppressed, with no formation of Al_4C_3 , thanks also to the small contact time between molten alloy and ceramic reinforcement. On the opposite, for laser melting process this was already observed by Ghosh et al. [87] and other literature works: it is probably due to the very high temperature achievable in the melt pools formation phase (above 1800 °C). As shown in the XRD spectrum reported in figure 5.26, the peaks of Al_4C_3 phase are evident under the much higher signals of Al and Si, whereas the SiC peaks are almost disappeared.

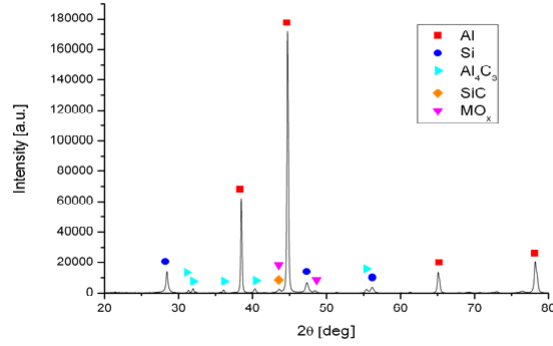


Figure 5.26: XRD spectrum of fabricated Al/SiC composite by DMLS

As a consequence, it was fundamental to take into account the occurring reaction in the system. The theoretical value of composite density had to be recalculated accordingly. In this way, it was possible to obtain new values of porosities which are even reduced with respect to the unreacted case presented before. As before, the results are summarized in a graph of total porosities values versus VED values (you can observe figure 5.27).

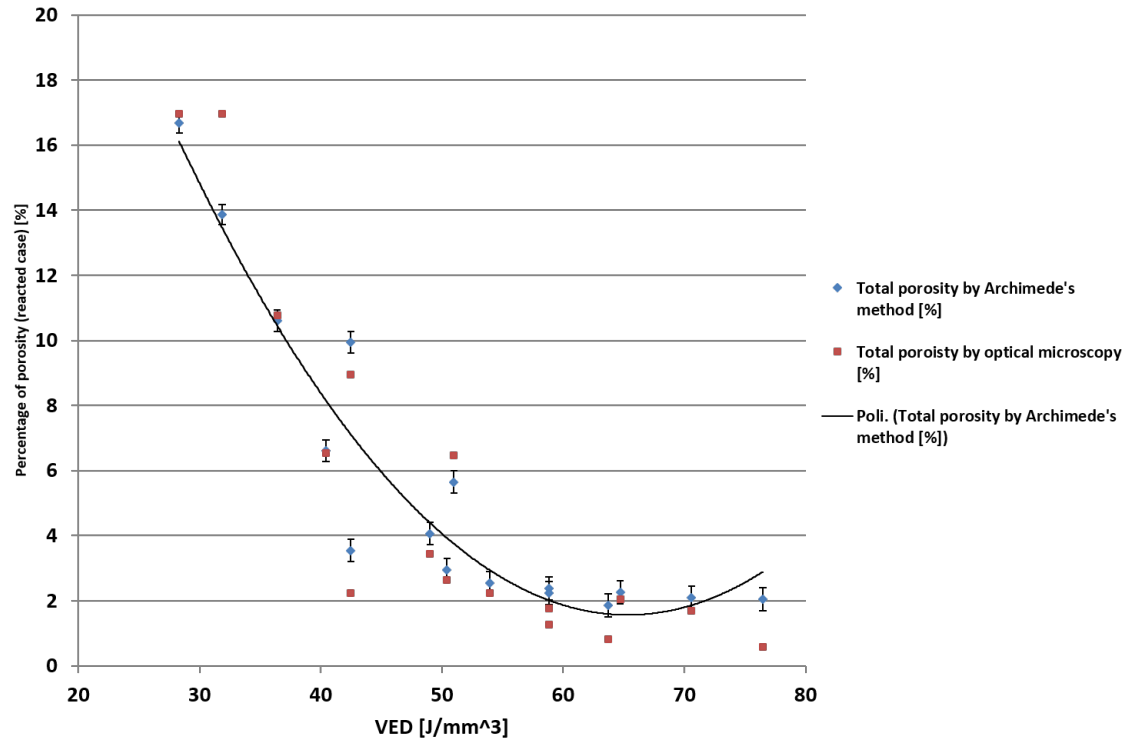


Figure 5.27: Percentage of total porosity obtained by the two used methods versus VED taking into account reaction (1)

Another issue had to be taken into account, concerning the evaluation of porosity. Some of the analysed samples presented a certain quantity of cracks, mostly solved through a geometrical optimization of the shape of the parts, such as the introduction of round corners instead of sharp corners (you can see examples of this in figure 5.28). These parts do no show anymore a visible crack density after grinding.

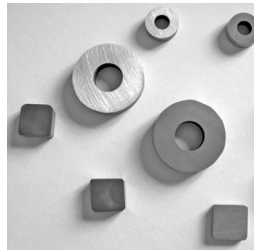


Figure 5.28: Examples of optimized shapes of composite parts

Another important parameter which was modified in order to reduce the stress concentrations in the material is the temperature of the building platform, which was arised from the default 35 °C up to 100 °C.

5.2.3 Mechanical properties evaluation

The elastic modulus E of the Al/SiC composite was evaluated by IMCE method on the same specimens which were fabricated for the bending tests. The specimens are illustrated in figure 5.29.

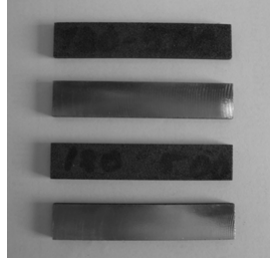


Figure 5.29: Al/SiC bending test specimens produced by DMLS

The obtained Young's modulus values are reported in the following table 5.13. The E modulus is higher with respect to the one of the AlSi10Mg alloy in comparable testing conditions (in particular in terms of surface finishing).

Sample I.D.	frequence [Khz]	E [GPa]	t/L	L/t	b/t	coeff. Poisson	correction factor extended method T1
180-500-1	10,45	80,2	0,08	12,15	2,64	0,33	1,05
180-500-2	8,81	83,2	0,08	13,32	2,60	0,33	1,04
180-500-3	8,58	84,6	0,07	13,61	2,61	0,33	1,04
180-500-4	8,51	82,2	0,07	13,56	2,58	0,33	1,04

Table 5.13: Young's modulus measurement by IMCE method

In addition to the Young's modulus, since the IMCE test is not destructive, three point bending tests were performed on the same composite specimens. The bending strength results are illustrated in the following table 5.14, whereas the figure 5.30 shows the stress-extension curves.

Sample I.D.	Archimede's density [g/cm ³]	Bulk density [g/cm ³]	Total Porosity (unreacted) [%]	Total Porosity (reacted) [%]	Young's Modulus [GPa]	Flexural strength [MPa]
180-500-1	2,593	2,589	4,3	3,3	83,8	501,6
180-500-2	2,609	2,604	3,8	2,7	81,7	531,6
180-500-3	2,605	2,601	3,9	2,8	83,3	504,0
180-500-4	2,608	2,606	3,7	2,6	78,0	525,6

Table 5.14: Three point bending tests results on Al/SiC composite by DMLS

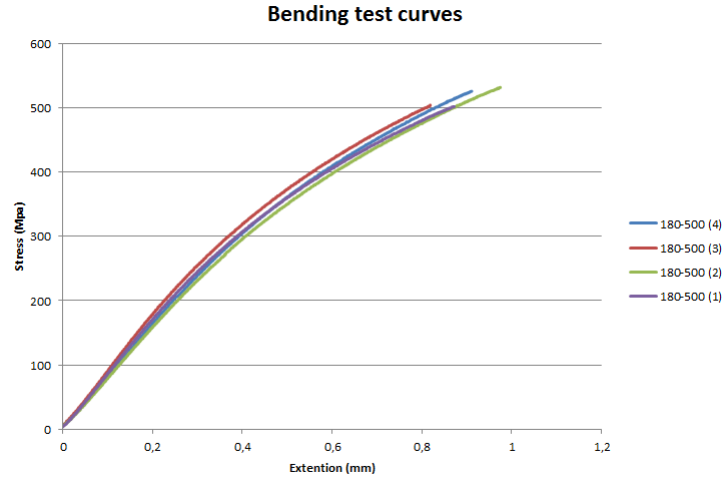


Figure 5.30: Bending test curves from Al/SiC composites by DMLS

5.2.4 Nanohardness characterization

In addition to the described mechanical characterization, nanohardness tests were carried out, since they could be useful to better understand the properties which are strictly dependent on the microstructure scale.

In figure 5.31 is reported an example of a 10x10 indentation pattern pursued on the surface of a mirror-like polished sample of AlSi10Mg alloy. The associated stress-strain curves are in the subsequent figure 5.32.

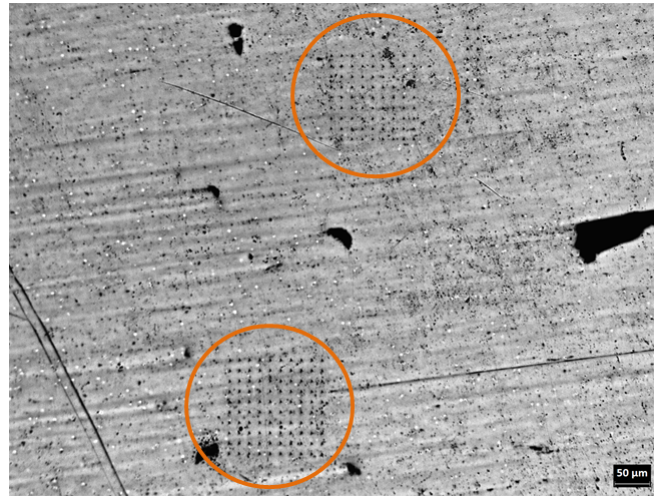


Figure 5.31: Example of a nanoindentation pattern on AlSi10Mg by DMLS

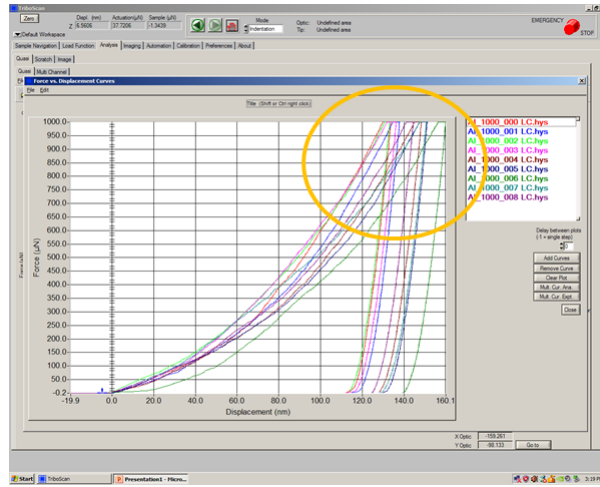


Figure 5.32: Family of stress-strain curves obtained after a 10x10 indentation test performed on an AlSiMg sample

By comparing the AlSi10Mg and SiC reinforced composites acquired indentation data (figure 5.33), it can be observed that many measurements were repeated at constant load to have a more reliable statistics of the results. The graph is particularly interesting because the nanoindentation measurements complete the hardness characterization at different length-scales (from nano to macro hardness).

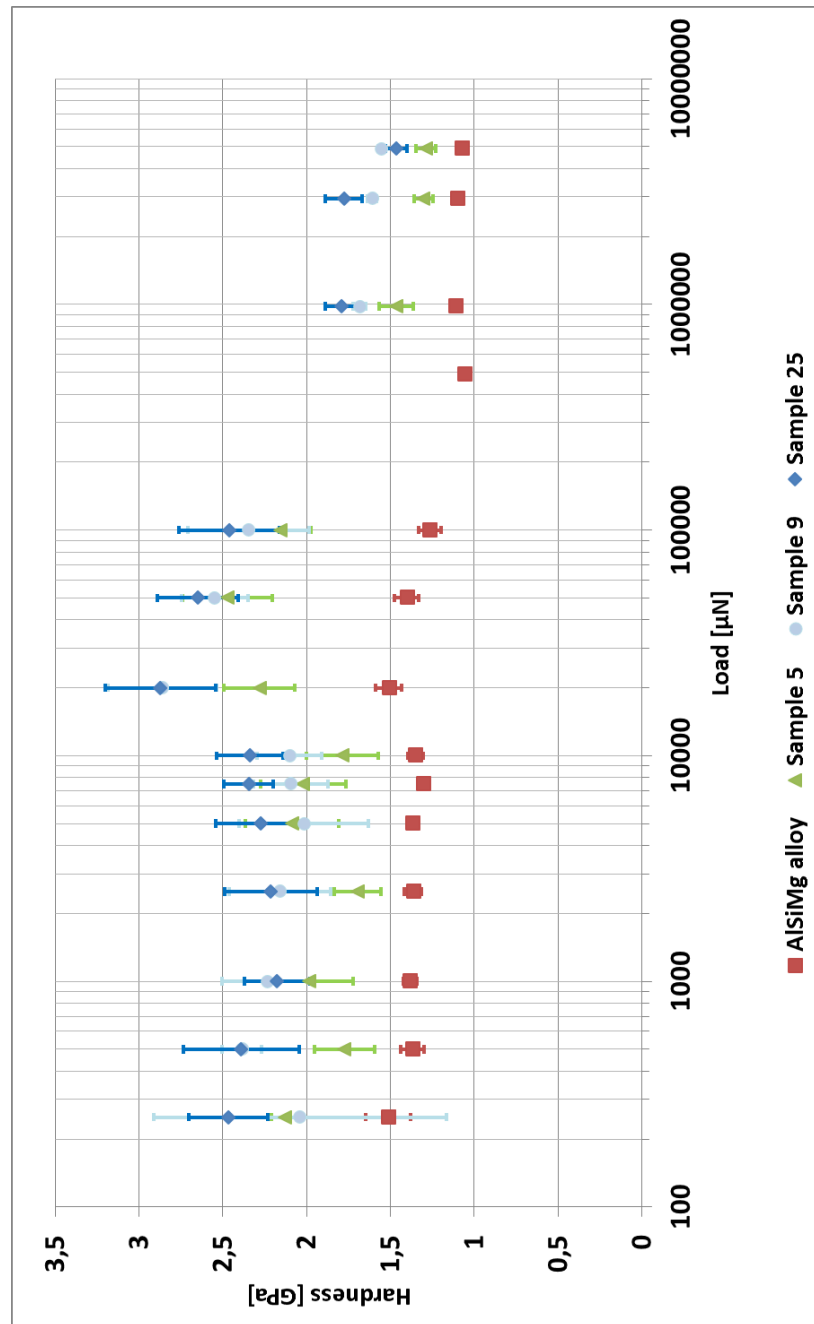


Figure 5.33: Hardness evaluation of AlSi10Mg alloy and the SiC reinforced composites by DMLS at different length-scales: from nano to micro to macro hardness

It can be clearly stated that the SiC reinforced composite samples present a higher hardness with respect to the Al (matrix) alloy. Samples 5, 9 and 25 were chosen in order to investigate the influence of different porosity levels on the hardness.

Moreover, the behaviour of the alloy is less fluctuating in terms of deviations from the mean values, whereas the composite tends to be more dependent on the area in which the indentation is performed. This could be attributed to the fact that in the composite different phases of different nature are present, and the structure so results to be less homogeneous with respect to the aluminum matrix alone.

5.2.5 Microstructural characterization

A dense sample for the microscopy observations was prepared by polishing along the building z direction with the metallographic polishing means, starting from abrasive SiC papers down to the silica diluted suspension. In order to enhance the microstructural elements it was subsequently chemically etched by the use of Weck's reagent.

The microstructure of the composite along the z direction sample is illustrated in the optical micrograph of figure 5.34.

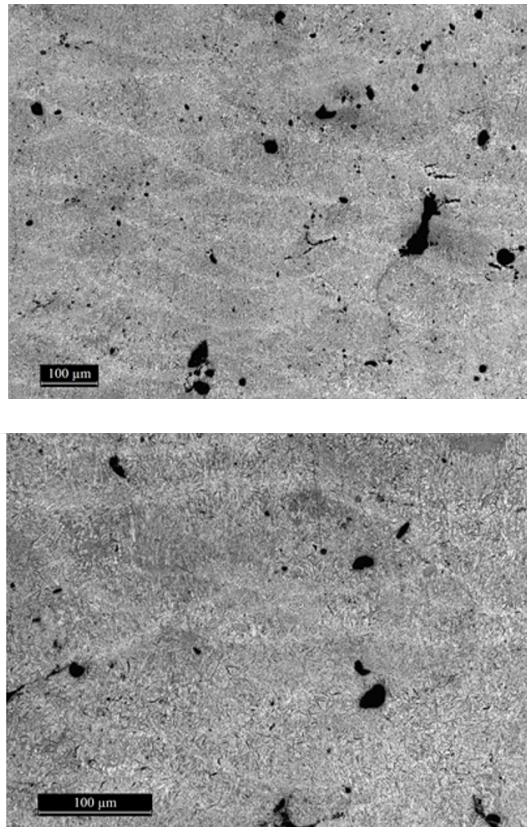


Figure 5.34: Al/SiC by DMLS optical micrographs at different magnifications

The microstructure is very fine and the laser signs are visible at lower magnifications, but the presence of SiC particles quite alters the aluminium alloy microstructure previously described. In particular it can be observed the presence of “dark” elongated acicular grains, which probably consist of some types of mixed oxides that form during DMLS process. At higher magnifications the characteristics of the microstructure can be appreciated more in detail, like in the micrograph shown in figure 5.35.

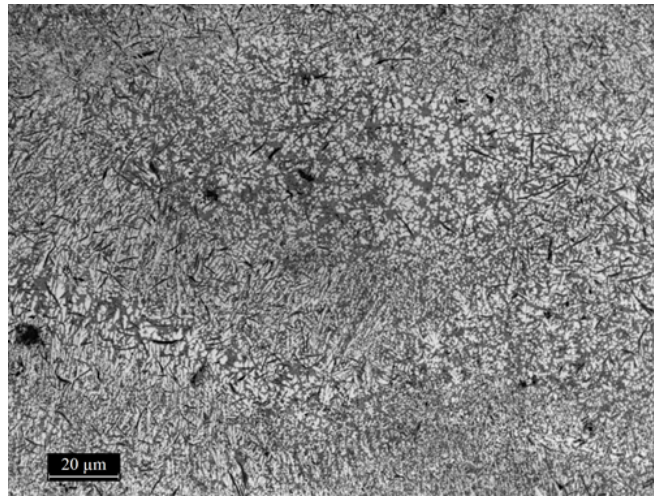


Figure 5.35: High magnification optical micrograph of Al/SiC by DMLS

From the micrograph you could distinguish submicrometric grains of Al (α) solid solution in form of dendrites, Si and other phases. The other phases are mainly carbides of variable compositions which form in - situ during the DMLS process.

In the FESEM micrographs the really fine dendritic structure becomes much more evident. This is due to the extremely fast solidification after the localized melting (figure 5.36). Some residual porosity is visible, and it could be also considered consequent to the poorer flowability of the composite powder with respect to the AlSi10Mg powder.

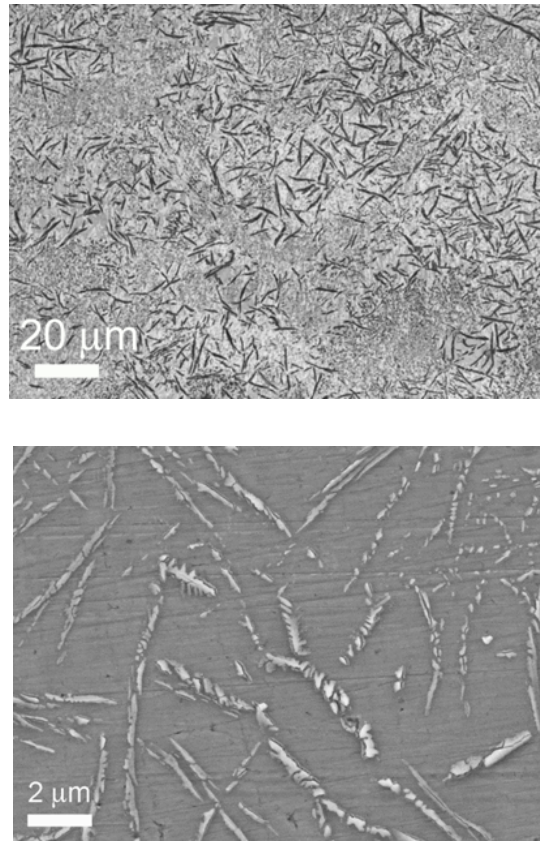


Figure 5.36: FESEM micrographs of Al/SiC composite by DMLS

Moreover it can be assumed that the size of Al_4C_3 phase after reaction (1) is sufficiently small to be unrecognizable also at a FESEM observation. Instead, the residual SiC phase could be detected only as agglomerate.

By using the same Berkovich tip which was used to characterize the hardness, in figure 5.37 an example of the Scanning Probe Microscopy (SPM) images, which were obtained by raster scanning the surface of a composite sample, is illustrated.

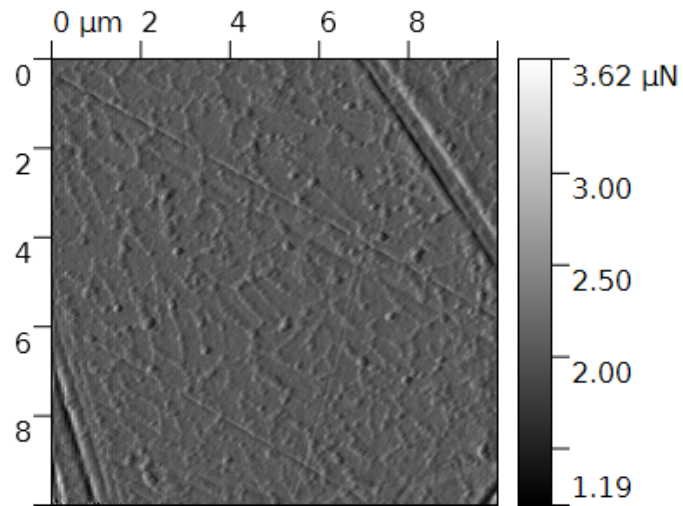


Figure 5.37: Example of the Scanning Probe Microscopy (SPM) imaging of Al/SiC composite sample number 25

These images contribute to confirm that the grain size of the phases which constitute the material is very fine.

5.3 AlSi10Mg/nanoMgAl₂O₄(0.5% in wt.) composite

Another ceramic reinforcement which was employed to investigate the feasibility of fabricating AMCs by DMLS in this PhD thesis work is represented by MgAl₂O₄. The reinforcing ceramic content was decreased from 2% down to 1% in weight, and a final optimal composition was found out with 0.5% in weight of nanospinel.

5.3.1 Starting material

In this case the ex situ approach was applied in the same way as it was pursued for SiC reinforced composite. The ceramic particles of MgAl₂O₄ had mean diameters ranging from 10 to 50 nm, and therefore they highly tended to agglomerate. A batch of powder of Mg-nanospinel was analysed by FESEM prior to the mixing operation (figure 5.38).

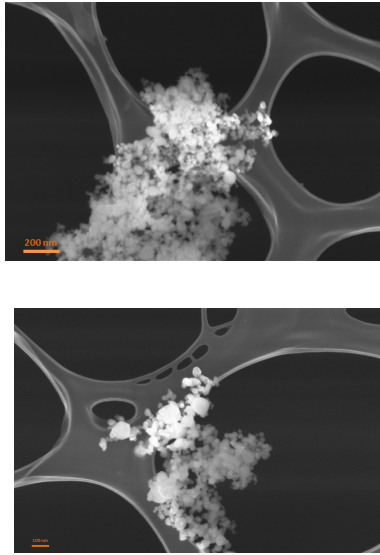


Figure 5.38: FESEM observation of Mg-nanospinel powder

After mixing the obtained composite powder was then analysed again by FESEM (figure 5.39). On the whole, the composite powder behaved very similarly to the Al alloy, confirming the choice of avoiding deformation of the metal during the mixing of the two powders. The increase of friction between composite powders due to the presence of the ceramic coating and to the interaction of the rough surfaces seems very limited in this case, due to the much larger ratio between the size of the metal and the ceramic particles in comparison with the

SiC reinforced composite. This is the consequence of the choice of a nanometric size of the ceramic phase.

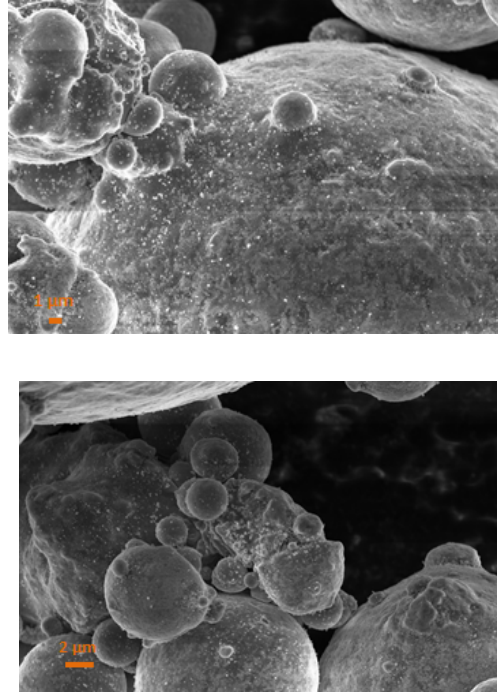


Figure 5.39: FESEM observation of Al/Mg-nanospinel powder after mixing

In addition, the morphology and the flowability do not change in comparison to the alloy alone.

5.3.2 Density and porosity evaluation

In the case of nanospinel AMC, the density results to be more dependent on the hatching distance compared to the laser power. Rectangular specimens of 15x15x10 mm dimensions were fabricated, as illustrated in figure 5.40. In this case the rule of mixture (you can find the used equation in the paragraph 5.2), provided a theoretical density of the composite equal to 2.685 g/cm^3 .

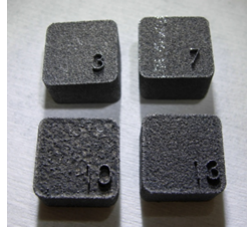


Figure 5.40: Al/Mg-nanospinel composite samples by DMLS

The porosities of the different composites fabricated with the different process parameters combinations, were evaluated by the same two methods used for the SiC composite: one based on the optical micrographs analysis and the other one based on the three weightings (in air, in distilled water and after drying). The results are shown in figure 5.41, where the total porosities values are plotted versus the VED values.

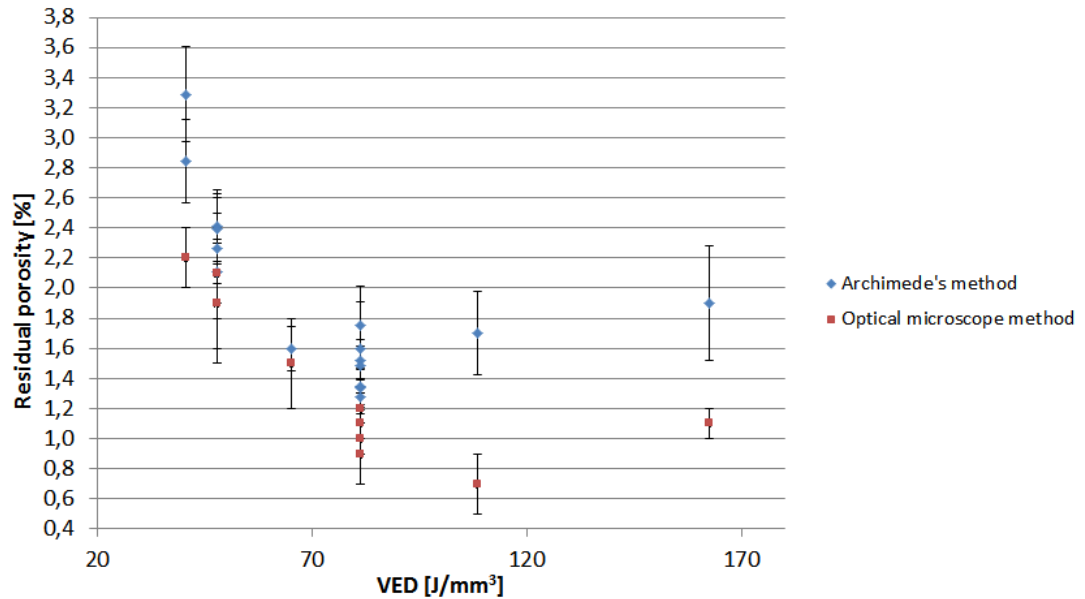


Figure 5.41: Percentage of porosity of AlSiMg/Mg-nanospinel versus VED

The trend followed by the experimental data is the same for the two methods. However there is not a very good superimposition of the porosity values for relatively high and low values of VED. Moreover, the two composites get a similar behaviour, if you compare the graph of figure with the above one. The operating range is clearly visible and it is evidenced with a circle.

5.3.3 Microstructural characterization

The microstructure of the AMC nanospinel composites is very similar to the aluminium matrix one, as illustrated in the micrographs of figure 5.42. As typical of the DMLS process the microstructure is very fine, made by submicrometric grains, elongated in the correspondence of the melt pools contour due to the heat transfer flux direction.

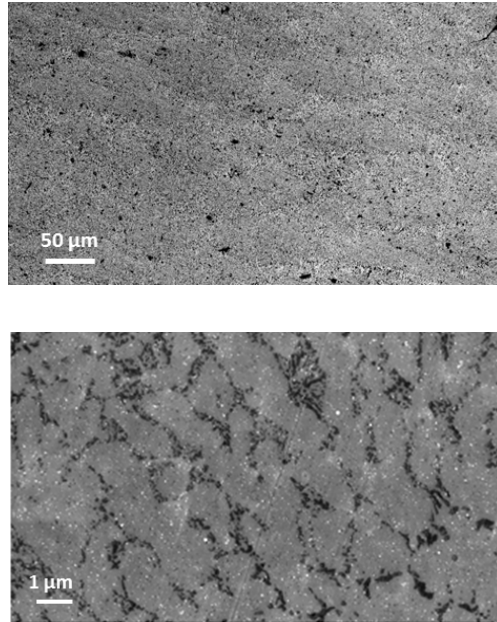


Figure 5.42: Optical (above) and FESEM (below) micrographs of AlSiMg/Mg-nanospinel composites by DMLS

For the nanospinel containing composite, the XRD analysis shows the presence of Al, Si, of the inter-metallic phase Mg_2Si and of some mixed metal-oxide ($AlSiO_x$). In the spectrum reported in figure 5.43, there is not the $MgAl_2O_4$ phase. This is reasonable because the nano-size originates very large but short peaks; moreover the spinel phase main peak is around 44.5° , so near the Al main one, and so could be covered by this. So with respect to the SiC containing composite, there are not new phases as reaction products. And it could be assumed that the phases detected in these composites are practically the same of the AlSiMg alloy after DMLS.

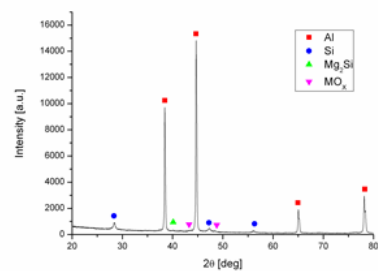


Figure 5.43: XRD analysis of nanospinel composite

Chapter 6

Conclusions

First of all the AlSi10Mg0.3 alloy was processed by DMLS and then deeply investigated with the aim to use it as matrix to develop Aluminum Matrix Composites (AMCs) by the same DMLS process.

The optimization of the process parameters was performed to determine the best “process window” based on the minimization of the residual level of porosity in function of the Volumetric Energy Density (VED).

The AlSi10Mg parts produced by DMLS process show a very fine microstructure with respect to the die cast aluminium alloy A360.2, which has a similar composition. Moreover, the AlSi10Mg parts processed by DMLS process show superior mechanical properties. The properties exhibit anisotropy along the building direction in comparison to the tests carried out along the plane. In addition, the surface finish condition of the specimen influences the mechanical properties of the material.

Regarding the composites, the AlSi10Mg0.3 powder was mechanically alloyed with 10%wt. of submicrometric SiC composite. First of all the residual level of porosity was contained at less than 5% and with respect to the results available in the literature for similar materials was a negligible value. The XRD characterization showed that a reaction between the matrix alloy and SiC particles occurred; anyway the composite hardness was doubled with respect to the Al matrix.

On the other side, regarding the nano MgAl_2O_4 reinforced composite, the material was successfully fabricated with residual porosities between 1.5 and 2%, and optimized like the other cited materials.

The main difference in comparison with the SiC reinforced composite is the mean size of the ceramic particles: this strongly affects the flowability of the processed material. In the case of the AlSiMg/Mg-nanospinel composite no reaction was detected between the matrix and the reinforcing ceramic phase, since this is an aluminum based oxide: this was confirmed by XRD analysis. The thermal expansion coefficient was reduced employing only 0.5% wt. of

nanoreinforcement in comparison to the matrix alone.

Future investigations

Future investigations could aim to complete the microstructural and mechanical characterization of the nano MgAl_2O_4 reinforced composite (0.5% in weight). In addition, other AMCs could be realized by the use of different nanoscale reinforcing ceramic phases, because of their reduced effect on the material flowability during the DMLS process, with respect to larger sizes of the reinforcement.

On the opposite, a completely different approach to fabricate composites by DMLS could be represented by the “in-situ” approach. Since the reinforcing phase is not mechanically added to the matrix but is instead generated during the fabrication process itself, the possible detrimental reactions between the two phases could be avoided.

Chapter 7

Bibliography

- [1] Wohlers T., Wohlers Report: Additive Manufacturing and 3D Printing State of the Industry, 2013.
- [2] <http://www.raeng.org.uk>
- [3] Manfredi D., Calignano F., Krishnan M., et al., Additive Manufacturing of Al Alloys and Aluminium Matrix Composites (AMCs), InTech, 2014.
- [4] Kruth. J.-P., Levy G., et al., Consolidation phenomena in laser and powder-bed based layered manufacturing, Annals of the CIRP Vol. 56/2/2007.
- [5] Krishnan M., Atzeni E., Canali R., Calignano F., Manfredi D., Ambrosio E.P., Iuliano L., On the effect of process parameters on properties of AlSi10Mg parts produced by DMLS, Rapid Prototyping Journal, Vol. 20 Iss. 6 (2014), 449 - 458.
- [6] N. Hopkinson, R. J. M. Hague, and P. M. Dickens, Rapid Manufacturing: An Industrial Revolution for the Digital Age, John Wiley & Sons Ltd, 2006.
- [7] F. W. Liou, Rapid Prototyping and Engineering Applications – A Toolbox for Prototype Development, CRC Press, Taylor & Francis Group LLC, 2008.
- [8] Goodridge, R. D.; Tuck, C. J.; Hague, R. J. M., Laser Sintering of Polyamide and other Polymers, Prog. Mater. Sci. 2012, 57 (2), 229–267.
- [9] Wiria, F. E.; Leong, K. F.; Chua, C. K., et al., Poly-ε-caprolactone/hydroxyapatite for Tissue Engineering Scaffold Fabrication by Selective Laser Sintering, Acta Biomater. 2007, 3 (1), 1–12.
- [10] Tan, K. H.; Chua, C. K.; Leong, K. F., et al., Scaffold Development Using Selective Laser Sintering of Polyetheretherketone-hydroxyapatite Biocomposite Blends, Biomaterials 2003, 24, 3115–3123.
- [11] Hao, L.; Savalani, M. M.; Zhang, Y, Effect of Material Morphology and Processing Conditions on the Characteristics of Hydroxyapatite and High-density Polyethylene Bio-composite by Selective Laser Sintering, Proc. Inst. Mech. Eng., Part L 2006, 220 (L3), 125–137.
- [12] Kim, J.; Creasy, T. S., Selective Laser Sintering Characteristics of Nylon 6/clay-reinforced Nanocomposite, Polym. Test. 2004, 23, 629–636.
- [13] Hon, B.; Gill, T., Selective Laser Sintering of SiC/Polyamide Composites, Ann. CIRP 2003, 52 (1), 173–176.

- [14] Zheng, H.; Zhang, J.; Lu, S., et al., Effect of Core-shell Composite Particles on the Sintering Behaviour and Properties of Nano- Al_2O_3 /polystyrene Composites Prepared by SLS, *Mater. Lett.* 2006, 60 (9–10), 1219–1223.
- [15] Mazzoli, A.; Moriconi, G.; Pauri, M. G., Characterization of an Aluminium-filled Polyamide Powder for Applications in Selective Laser Sintering, *Mater. Des.* 2007, 28 (3), 993–1000.
- [16] Beer, D. J. D.; Booyesen, G. J., Rapid Tooling Using Alumide, In *Proceedings of VRAP*, Leiria, Portugal, 2005; pp 387–394.
- [17] Tarasova, E. Y.; Kryukova, G. V.; Petrov, A. L., et al., Structure and Properties of Porous PZT Ceramics Synthesized by Selective Laser Sintering, *Method. Proc. SPIE* 2000, 3933, 502–504. 42.
- [18] Wilkes, J.; Wissenbach, K., Rapid Manufacturing of Ceramic Components for Medical and Technical Applications via Selective Laser Melting, In *Proceedings of the Euro- uRapid*, Frankfurt, 2006; p A4(1).
- [19] Casalino, G.; De Filippis, A. C.; Ludovico, A. A, Technical Note on the Mechanical and Physical Characterization of Selective Laser Sintered Sand for Rapid Casting, *J. Mater. Process. Technol.* 2005, 166 (1), 1–8.
- [20] Goodridge, R. D.; Wood, D. J.; Ohtsuki, C.; Dalgarno, K. W., Biological Evaluation of an Apatite-mullite Glass-ceramic Produced via Selective Laser Sintering, *Acta Biomater.* 2007, 3 (2), 221–231.
- [21] Frazier W. E., Metal Additive Manufacturing: A Review, *Journal of Materials Engineering and Performance*, 2014, vol. 23 (6), 1917–1928.
- [22] <http://www.arcam.com>
- [23] Gebhardt A., Understanding Additive Manufacturing, Institute for Advanced Fabrication Technologies and Additive Manufacturing, FH Aachen University of Applied Sciences, Aachen, Germany, 2011.
- [24] X. Gong, T. Anderson, and K. Chou, Review on Powder-based Electron Beam Additive Manufacturing Technology, *Proceedings of the ASME 2012 International Symposium on Flexible Automation*, 2012, pp. 1–9.
- [25] W. Hofmeister, M. Wert, J. Smugeresky, J. A. Philliber, M. Griffith, and M. Ensz, Investigating Solidification with the Laser-Engineered Net Shaping (LENS) Process, *JOM*, vol. 51, no. 7, 1999.
- [26] M. Zhong and W. Liu, Laser surface cladding: The state of the art and challenges, *Proc. Inst. Mech. Eng. Part C J. Mech. Eng. Sci.*, vol. 224, no. 5, pp. 1041–1060, 2010.
- [27] E. C. Santos, M. Shiomi, K. Osakada, and T. Laoui, Rapid manufacturing of metal components by laser forming, *Int. J. Mach. Tools Manuf.*, vol. 46, no. 12–13, pp. 1459–1468, 2006.
- [28] S. Kumar and S. Pityana, Laser-based additive manufacturing of metals, *Adv. Mater. Res.*, vol. 227, pp. 92–95, 2011.
- [29] Das, S. Physical Aspects of Process Control in Selective Laser Sintering of Metals. *Adv. Eng. Mater.* 2003, 5, 701–711.
- [30] Ferrar, B.; Mullen, L.; Jones, E., et al. Gas Flow Effects on Selective Laser Melting (SLM) Manufacturing Performance. *J. Mater. Process. Technol.* 2012, 212, 355–364.

- [31] Calignano F, Manfredi D, Ambrosio E.P., Iuliano L, Fino P., Influence of process parameters on surface roughness of aluminum parts produced by DMLS. *Int. J. Adv. Manuf. Technol.* 2013; 67 (9–12): 2743–2751.
- [32] Fischer P., Romano V. et al., Sintering of commercially pure titanium powder with a Nd:YAG laser source, *Acta Materialia* 51, 2003, 1651–1662.
- [33] Zaeh M. F., Branner G., Investigation on residual stresses and deformations in selective laser melting, *Prod. Eng. Res. Devel.* 4 (2010), 35–45.
- [34] Williams J. D., Deckard C. R., Advances in modeling the effects of selected parameters on the SLS process, *Rapid Prototyping Journal*, Volume 4, Number 2, 1998, pp. 90–100.
- [35] I. Gibson, W. D. Rosen, and B. Stucker, *Additive Manufacturing Technologies Rapid Prototyping to Direct Digital Manufacturing*. Springer, 2010.
- [36] J. P. Kruth, P. Marcellis, L. Froyen, and M. Rombouts, Binding Mechanisms in Selective Laser Sintering and Selective Laser Melting, in *Proceedings of Solid Freeform Fabrication symposium*, 2004, pp. 44–59.
- [37] Vilaro, T.; Colin, C.; Bartout, J. D., et al. Microstructural and Mechanical Approaches of the Selective Laser Melting Process Applied to a Nickel-base Superalloy. *Mater. Sci. Eng., A* 2012, 534, 446–451.
- [38] Sercombe, T.; Jones, N.; Day, R.; Kop, A. Heat Treatment of Ti-6Al-7Nb Components Produced by Selective Laser Melting. *Rapid Prototyping J.* 2008, 14 (5), 300–304.
- [39] Buchbinder D., et al., High Power Selective Laser Melting (HP SLM) of Aluminum Parts, *Physics Procedia* 12 (2011) 271–278.
- [40] Gusarov A. V., Smurov I., Modeling the interaction of laser radiation with powder bed at selective laser melting, *Physics Procedia* 5 (2010) 381–394.
- [41] Yadroitsev I., Gusarov A., Yadroitsava I., Smurov I., Single track formation in selective laser melting of metal powders, *Journal of Materials Processing Technology*, vol. 210, issue 12, (2010) 1624–1631.
- [42] Vrancken, B.; Thijs, L.; Kruth, J. P.; Van Humbeeck, J. Heat treatment of Ti6Al4V produced by Selective Laser Melting: Microstructure and mechanical properties, *J. of Alloys and Compounds* 541, 212, 177–185.
- [43] Yadroitsev, I.; Krakhmalev, P.; Yadroitsava, I. Selective laser melting of Ti6Al4V alloy for biomedical applications: Temperature monitoring and microstructural evolution, *J. of Alloys and Compounds* 583, 2014, 404–409.
- [44] Jia Q., Gu D., Selective laser melting additive manufactured Inconel 718 superalloy parts: High-temperature oxidation property and its mechanisms, *Optics and Laser Technology* 62, 2014, 161–171.
- [45] Kanagarajah, P.; Brenne, F.; Niendorf, T. et al. Inconel 939 processed by selective laser melting: Effect of microstructure and temperature on the mechanical properties under static and cyclic loading, *Materials Science and Engineering A* 588, 2013, 188–195.
- [46] Song B., Dong S. et al. Fabrication of NiCr alloy parts by selective laser melting: Columnar microstructure and anisotropic mechanical behavior, *Materials and Design* 53, 2014, 1–7.
- [47] Monroy K., Delgado J., Ciurana J. Study of the pore formation on

CoCrMo alloys by selective laser melting manufacturing process, *Procedia Engineering* 63, 2013, 361-369.

[48] Shyshkovsky, I.; Yadroitsev, I.; Smurov, I. Direct selective laser melting of nitinol powder, *Physics Procedia* 39, 2012, 447-454.

[49] Simchi, A. The Role of Particle Size on the Laser Sintering of Iron Powder. *Metall. Mater. Trans. B* 2004, 35, 937-948.

[50] Simchi, A.; Direct laser sintering of metal powders: Mechanism, kinetics and microstructural features, *Materials Science and Engineering A* 428, 2006, 148-158.

[51] Murali K., Chatterjee A. N., Saha, P. et al. Direct selective laser sintering of iron-graphite powder mixture, *Journal of Materials Processing Technology* 136, 2003, 179-185.

[52] Kruth J.P., Froyen L., Vaerenbergh J.V., Mercelis P., Rombouts M., Lauwers B. Selective laser melting of iron-based powder, *Journal of Materials Processing Technology* 149, 2004, 616-622.

[53] Song B., Dong S. et al. Microstructure and tensile properties of iron parts fabricated by selective laser melting, *Optics and Laser Technology* 56, 2014, 451-460.

[54] Yan C., Hao L., Hussein A., et al. Advanced lightweight 316L stainless steel cellular lattice structures fabricated via selective laser melting, *Materials and design* 55, 2014, 533-541.

[55] Liu Z. H., Zhang D. Q., et al. Crystal structure analysis of M2 high speed steel parts produced by selective laser melting, *Materials Characterization* 84, 2013, 72-80.

[56] Zhang D. Q., Entwicklung des Selective Laser Melting (SLM) für Aluminiumwerkstoffe. Dissertation, RWTH Aachen, 2001.

[57] Brandl E., Heckenberger U., Holzinger V., Buchbinder D. Additive manufactured AlSi10Mg samples using selective laser melting (SLM): microstructure high cycle fatigue, and fracture behaviour, 2012, *Materials & Design* 34, 159-169.

[58] Olakanmi, E.O., Cochrane, R.F., Dalgarno, K.W. Spheroidisation and oxide disruption phenomena in direct Selective Laser Melting (SLM) of pre-alloyed Al-Mg and Al-Si powders, 2009, in *TMS Annual Meetings and Exhibition proceedings*, USA, pp. 371-380.

[59] Olakanmi, E.O., Cochrane, R.F., Dalgarno, K.W. Densification mechanism and microstructural evolution in selective laser sintering of Al-12Si powders, 2011, *Journal of Materials Processing Technology* 211 (1), 113-121.

[60] Thijs L., Kempen K., Kruth J. P., Van Humbeeck J. Fine-structured aluminium products with controllable texture by selective laser melting of pre-alloyed AlSi10Mg powder, 2013, *Acta Materialia* 61, 1809-1819.

[61] Y. Zhang, A. Faghri, Melting of a subcooled mixed powder bed with constant heat flux heating, *Int. J. Heat Mass Transfer* 42 (1999) 775-788.

[62] S. Kolossov, E. Boillat, R. Glardon, P. Fischer, M. Locher, 3D FE simulation for temperature evolution in the selective laser sintering process, *Int. J. Machine Tools Manufact.* 44 (2004) 117-123.

- [63] K. Dai, L. Shaw, Thermal and mechanical finite element modeling of laser forming from metal and ceramic powders, *Acta Mater.* 52 (2004) 69–80.
- [64] H. Chung, S. Das, Numerical modeling of scanning laser-induced melting, vaporization and resolidification in metals subjected to step heat flux input, *Int. J. Heat Mass Transfer* 47 (2004) 4153–4164.
- [65] J.C. Nelson, Selective laser sintering: a definition of the process and an empirical sintering model, Ph.D. dissertation, University of Texas, Austin, TX, 1993.
- [66] M.M. Sun, Physical modeling of the selective laser sintering, Ph.D. dissertation, University of Texas, Austin, TX, 1991.
- [67] M. Cervera, G. Lombera, Numerical prediction of temperature and density distributions in selective laser sintering processes, *Rapid Prototyping J.* 5 (1) (1999) 21–26.
- [68] D.L. Bourell, H.L. Marcus, J.W. Barlow, J.J. Beaman, Selective laser sintering of metals and ceramics, *Int. J. Powder Metall.* 28 (4) (1992) 369–381.
- [69] Manfredi D., Calignano F., Krishnan M., Canali R., Ambrosio E. P., Atzeni E., From Powders to Dense Metal Parts: Characterization of a Commercial AlSiMg Alloy Processed through Direct Metal Laser Sintering, *Materials* 2013, 6(3), 856–869.
- [70] Kruth, J.-P.; Duflou, J.; Mercelis, P., et al. On-line Monitoring and Process Control in Selective Laser Melting and Cutting. In *Proceedings of the LANE 2007*, Vol. 5; 2007; pp 23–37.
- [71] Craeghs, T.; Bechmann, F.; Berumen, S., et al. Feedback Control of Layerwise Laser Melting Using Optical Sensors. *Phys. Procedia* 2010, 5, 505–514.
- [72] Tolochko, N. K.; Laoui, T.; Khlopkov, T. V., et al. Absorptance of Powder Materials Suitable for Laser Sintering. *Rapid Prototyping J.* 2000, 6 (3), 155–166.
- [73] Glardon, R.; Karapatis, N.; Romano, V. Influence of Nd: YAG Parameters on the Selective Laser Sintering of Metallic Powders. *Ann. CIRP* 2001, 50 (1), 133–136.
- [74] Savalani, M. M.; Hao, L.; Harris, R. A. Evaluation of CO₂ and Nd: YAG Lasers for the Selective Laser Sintering of HAPEX(R). *Proc. Inst. Mech. Eng., Part B* 2006, 220 (2), 171–182.
- [75] Rombouts, M.; Kruth, J.-P.; Froyen, L.; Mercelis, P., Fundamentals of Selective Laser Melting of Alloyed Steel Powders., *Ann. CIRP* 2006, 55 (1), 187–192.
- [76] Ghany K. A., Moustafa S. F., Comparison between the products of four RPM systems for metals, *Rapid Prototyping Journal* 12/2 (2006) 86–94.
- [77] <http://www.eos.info/en>
- [78] Gebhardt A., et al., Additive Manufacturing by selective laser melting the realizer desktop machine and its application for the dental industry, *Laser Assisted Net Shape Engineering* 6, *Proceedings of the LANE 2010*, Part 2.
- [79] Simchi A., Pohl H., Direct laser sintering of iron graphite powder mixture, *Mater. Sci. Eng. A* 2004;383(2):191–200.
- [80] Laoui T., Froyen L., Kruth J.-P., Effect of mechanical alloying on selective laser sintering of WC-Co powder, *Powder Metal.* 2000;42(3):203–5.

- [81] Maeda K., Childs T., Laser sintering (SLS) of hard metal powders for abrasion resistant coatings, *J. Mater. Process. Technol.* 2004;149(13):609-15.
- [82] Gu D, Shen Y. WC-Co particulate reinforcing Cu matrix composites produced by direct laser sintering, *Mater. Lett.* 2006;60(2930):3664-8.
- [83] Gaard A., Krakhmalev P., Bergstrom J., Microstructural characterization and wear behaviour of (Fe,Ni)TiC MMC prepared by DMLS, *J. Alloys Comp.* 2006;421(12):166-71.
- [84] Topcu I., Gulsoy H. O., et al., Processing and mechanical properties of B₄C reinforced Al matrix composites, *Journal of Alloys and Compounds* 482, (2009) 516-521.
- [85] Kerti I., Toptan F., Microstructural variations in cast B₄C-reinforced aluminium matrix composites (AMCs), Volume 62, Issues 89, 31 (2008), 1215-1218.
- [86] Simchi A., Godlinski D., Effect of SiC particles on the laser sintering of Al7Si0.3Mg alloy, *Scripta Materialia* 59 (2008) 199-202.
- [87] Ghosh S.K., Saha P., Crack and wear behavior of SiC particulate reinforced aluminium based metal matrix composite fabricated by direct metal laser sintering process, *Materials and Design* 32 (2011) 139-145.
- [88] Leong, C. C.; Lu, L.; Fu, J. Y. H.; Wong, Y. S. In-situ Formation of Copper Matrix Composites by Laser Sintering. *Mater. Sci. Eng., A* 2002, 338, 81-88.
- [89] Lu, L.; Fu, J. Y. H.; Chen, Z. D., et al. In-situ Formation of TiC Composite Using Selective Laser Melting. *Mater. Res. Bull.* 2000, 35, 1555-1561.
- [90] Slocombe, A.; Li, L. Selective Laser Sintering of TiC-Al₂O₃ Composite with Self-propagating High-temperature Synthesis. *J. Mater. Process. Technol.* 2001, 118, 173-178.
- [91] Kamitani, T.; Yamada, O.; Marutani, Y. Selective Laser Sintering with Heat of Formation by Using Reactive Materials. *Proc. SPIE* 2000, 4808, 299-302.
- [92] Shishkovskii, I. V.; Tarasov, E. Y.; Zhuravel, L. V.; Petrov, A. L. Selective Laser Sintering in the Powder Synthesis of a Biocomposite Based on Titanium Nickelide and Hydroxyapatite. *Tech. Phys. Lett.* 2001, 27 (3), 211-213.
- [93] Spierings A. B., Schneider M., Comparison of density measurement techniques for additive manufactured metallic parts, *Rapid Prototyping Journal* 17/5, 2011, 380-386.
- [94] Lucca D.A., Herrmann K., Klopstein M. J., Nanoindentation: Measuring methods and applications, *CIRP Annals - Manufacturing Technology*, Volume 59, Issue 2, 2010, Pages 803-819.
- [95] Oliver W. C. and Pharr G. M., Measurement of hardness and elastic modulus by instrumented indentation: Advances in understanding and refinements to methodology, *J. Mater. Res.*, 2004, vol. 19, no. 1, pp. 3-20.
- [96] Davis J. R., editor for *ASM Specialty Handbook: Aluminum and Aluminum Alloys*

- [97] Manfredi D., Calignano F., Ambrosio E. P., Krishnan M., Canali R., Biamino S., Pavese M., Atzeni E., Iuliano L., Fino P., Badini C., Direct Metal Laser Sintering: an additive manufacturing technology ready to produce lightweight structural parts for robotic applications, *La Metallurgia Italiana* n.10, 2013, pp. 15-24.
- [98] Krishnan M., Atzeni E., Canali R., Manfredi D., Calignano F., Ambrosio E. P., Iuliano L., Influence of post-processing operations on mechanical properties of AlSi10Mg Parts by DMLS, *Proceedings of VRAP International Conference*, Leiria, 2013.
- [99] El-Kady O., Fathy A., Effect of SiC particle size on the physical and mechanical properties of extruded Al matrix nanocomposites, *Materials and Design* 54, 2014, pp. 348-353.
- [100] Lee J. C., et al., Prediction of Si contents to suppress the formation of Al₄C₃ in the SiCp/Al composite, *Acta Materialia*, vol. 46 no. 5, pp. 1771-180, 1998.
- [101] <http://www.hcstarck.com/en/home.html>